UNIVERSITY OF OKLAHOMA

GRADUATE COLLEGE

IMPROVING FAULT IMAGES USING A DIRECTIONAL LAPLACIAN OF A GAUSSIAN OPERATOR

A THESIS

SUBMITTED TO THE GRADUATE FACULTY

in partial fulfillment of the requirements for the

Degree of

MASTER OF SCIENCE

By

GABRIEL MACHADO ACOSTA
Norman, Oklahoma
2016

IMPROVING FAULT IMAGES USING A DIRECTIONAL LAPLACIAN OF A GAUSSIAN OPERATOR

A THESIS APPROVED FOR THE
CONOCOPHILLIPS SCHOOL OF GEOLOGY AND GEOPHYSICS

BY

_____
Dr. Kurt Marfurt, Chair

_____
Dr. Roger Slatt

_____
Dr. John Pigott

To my dear family, and those friends that more than friends, but are like family to me.

To all of you.

Acknowledgements

I would like to thank the sponsors of the Attribute-Assisted Seismic Processing and Interpretation Consortium for their guidance and financial support. I would also like to thank Schlumberger for providing Petrel licenses used in the current research paper. Finally, the NZPAM for providing access to their data to the geoscience community at large.

Table of Contents

Acknowledgements iv

List of Figures vi

Abstract xi

Chapter 1: Directional Laplacian of a Gaussian theory 1

Eigenvector estimation of fault dip and azimuth 1

Fault smoothing and edge enhancement using the directional Laplacian of a Gaussian operator 3

Directional smoothing and sharpening 4

Chapter 2: dLoG application on two New Zealand basins 7

Great South Basin 7

Canterbury Basin 16

Chapter 3: dLoG as a preconditioner for ant-tracking and automatic fault picking 22

The ant-tracking algorithm 22

Fault object extraction 32

Chapter 4: Conclusions 39

References 40

Appendix: Geologic Background of the Great South Basin 42

List of Figures

Figure 1. Cartoon showing reflectors (as solid red lines) and a coherence anomaly (as black dotted line). The analysis window (in green) is a circle centered on the analysis point (in orange). The eigenvector v_3 is perpendicular to the fault plane reflector (blue arrow), while the normal vector n is perpendicular to the reflector (red arrow). The dLoG operator (red negative and blue positive) is short in the direction parallel to v_3 and three times longer in the direction parallel to v_1 and v_2 5

Figure 2. Time slice at t= 2.52 s through co-rendered fault dip-azimuth, fault dip-magnitude and LoG filtered coherence (fault probability). The fault probability is plotted against lightness, with low values opaque (white) and high values transparent. ..6

Figure 3. (a) Time slice at t=2.52 s and (b) vertical slice along AA' through a seismic amplitude volume with a bin size of 12.5 by 25 m.....8

Figure 4. (a) Time slice at *t*=2.52 s and (b) vertical slice along AA' through a coherence volume computed from the seismic amplitude data shown in Figure 3. The orientation of the coherence anomalies in (a) are shown on Figure 2. 9

Figure 5. (a) Time slice at *t*=2.52 s and (b) vertical slice along AA' through the directional dLoG attribute computed from the coherence volume shown in Figure 5. (c) Filter applied to coherence computed from the dip magnitude of v_3 that suppresses features parallel to reflector dip. Block blue arrows indicate faults that are now more continuous and easier to identify. 11

Figure 6. Time slice at *t*=2.52 s through co-rendered fault dip-azimuth, fault dip-magnitude, fault probability and seismic amplitude. The fault dip magnitude and azimuth are computed from v_3. The opacity used for each attribute is displayed on top

of the color bar. Fault dip azimuth is plotted against a cyclical color bar, fault dip magnitude against a monochrome gray scale, the dLoG attribute against a monochrome white scale and seismic amplitude against a black and white binary color bar. Fault dip azimuth and magnitude can be easily characterized through this combination of attributes. Sharpened events sub parallel to the vertical slices appear smeared (blue and yellow on the N-S line, red and green on the E-W line). 13

Figure 7. (a) Time slice at *t*= 2.8 s through co-rendered fault dip-azimuth, fault dip-magnitude, fault probability and seismic amplitude. The fault dip magnitude and azimuth are computed from v_3. The opacity used for each attribute is displayed on top of the color bar. Fault dip azimuth is plotted against a cyclical color bar, fault dip magnitude against monochrome gray the fault probability attribute against monochrome white and seismic amplitude against a black and white dipole color bar. Shale dewatering features are pointed with the blue block arrow. (b) and (c) show two vertical lines with orthogonal orientation and the seismic image of the shale dewatering features with an outward dipping trend. 15

Figure 8. Time slice at *t*=2.04 s through a) coherence, b) dLoG of coherence fault probability c) co-rendered fault dip-azimuth, fault dip-magnitude and dLoG of coherence ("fault" probability). The fault dip magnitude and azimuth are computed from v_3. The transparency function used for each attribute is displayed on top of the color bar. Fault dip azimuth is plotted against a cyclical color bar, fault dip magnitude against a monochrome gray color bar, fault probability against a monochrome white color bar. Channel features are easily recognized through the conventional coherence,

but sharpened and cleaner after dLoG filtering. The channel edges are further characterized by combining with fault dip magnitude and azimuth attributes. 17
Figure 9. Time slice at *t*= 2.52 s through faults shown in Figure 6 highlighting near horizontal discontinuities through the use of a taper which hinders any feature with a dip greater than 25°.....18
Figure 10. Time slice at *t*= 2.52 s through faults corresponding to Figure 6 with a dip magnitude filter that reflects features whose dip is less than 65°.....19
Figure 11. 3D view of two vertical lines through the seismic amplitude volume, and a box probe through co-rendered fault dip azimuth and fault dip magnitude showing polygonal faulting. The fault probability modulates the opacity, where vowels with $\alpha<0.5$ are being rendered transparent. Lineaments that are less than 25° of dip to the reflector have been filtered out. 20
Figure 12. The same image as Figure 11, but now with faults with N and S azimuths rendered transparent. Thus a synthetic and antithetic fault system is highlighted 21
Figure 13. A model of how real ants find the shortest path. (a) Ants arrive at a decision point. (b) Some ants choose the upper path and some the lower path. The choice is random. (c) Since the ants move at approximately a constant speed, the ants that choose the lower, shorter, path reach the opposite decision point faster than those that choose the upper, longer, path. (d) Pheromone accumulates at a higher rate on the shorter path due to a higher amount of ants crossing it. The number of dashed lines is approximately proportional to the amount of pheromone deposited by ants (taken from Dorigo et al., 1997).....23

Figure 14. (a) Time slice through a fault attribute (variance) with (b) corresponding ant tracking results (after Iske et al., 2005). 24
Figure 15. Seismic amplitude of survey from the Taranaki Basin. Relatively flat geology on top of normally faulted sequences below 1500 ms. Block arrow indicates an unconformity. 25
Figure 16. The same vertical section from Figure 15 through (a) variance attribute and (b) corresponding ant-tracked attribute. The stereonet shows that ants were constrained to search within a cone of 30° about the vertical (fault dips > 60°). 26
Figure 17. The same vertical slice shown in Figure 15 through (a) Energy Ratio Similarity attribute and (b) corresponding ant-track attribute. Note noise in the upper right region of the right image. 27
Figure 18. The same vertical slice shown in Figure 15 through (a) first iteration of LoG attribute and (b) corresponding ant-track attribute. Note noise diminishment in the upper right region of the right image. 28
Figure 19. The same vertical slice shown in Figure 15 through (a) fault probability after the third iteration of dLoG filtering and (b) corresponding ant-track attribute. Note noise diminishment in the upper right region of the right image and improved fault resolution. 29
Figure 20. Workflow for automatic fault object extraction. 33
Figure 21 (a) Seismic cross-section showing three manually picked faults that are displayed (b) in 3D. Time slice is through the dLoG attribute fault probability. 36
Figure 22. Fault extraction patches (left) for LoG, variance and energy ratio similarity. The histograms to the right represent the patches sorted by surface area. 37

Figure 23. Histogram showing the similarity of computer-assisted fault extraction to manually extracted faults shown in Figure 21 for faults generated using (a) LoG and (b) variance. 38

Abstract

Fault picking is a critical, but human-intensive component of seismic interpretation. In a bid to improve fault imaging in seismic data, I have applied a directional Laplacian of a Gaussian (dLoG) operator to sharpen fault features within a coherence volume. I compute an *M* by *M* matrix of the second moment distance-weighted coherence tensor values that fall within a 3D spherical analysis window about each voxel. The eigenvectors of this matrix define the orientation of planar discontinuities while the corresponding eigenvalues determine whether these discontinuities are significant. The eigenvectors, which quantify the fault dip-magnitude and dip-azimuth, define a natural coordinate system for both smoothing and sharpening the planar discontinuity. By comparing the vector dip of the discontinuity to the vector dip of the reflectors, I can apply a filter to either suppress or enhance discontinuities associated with unconformities or low signal-to-noise ratio shale-on-shale reflectors. Such suppression become useful in the implementation of subsequent skeletonization algorithms. Automatic fault picking processes for accelerated interpretation of basins also become much easier to implement and more accurate. I demonstrate the value and robustness of the technique through application to two 3D post stack data volumes from offshore New Zealand, which exhibit polygonal faulting, shale dewatering, and mass-transport complexes. Finally, I use these filtered faults as input to an ant-tracking algorithm and automatic fault extraction and find significant improvement in the speed and accuracy of fault interpretation.

Chapter 1: Directional Laplacian of a Gaussian theory

The next section is extracted from Machado et al (2016).

Eigenvector estimation of fault dip and azimuth

This work is based on Barnes' (2006) contribution to edge detection methods, where he constructed a second moment tensor using an edge attribute, $\alpha_{m,} = 1 - c_m$, where c_m is coherence, with an *M*-voxel analysis window

$$C_{ij} = \frac{\sum_{m=1}^{M} x_{im} x_{jm} \alpha_m}{\sum_{m=1}^{M} \alpha_m}, \quad (1)$$

where the variables x_{im} *and* x_{jm} are the distances from the center of the analysis window along axis *i* and *j* of the m^{th} data point respectively. In order to numerically support the dLoG operator, the analysis window needs to include at least seven traces along the x and y-axes, thereby defining a sphere of points in *x*, *y* and z where the *z* axis defines depth converted samples.

In the absence of an anomaly the value of α_m in equation 1 will be zero. In a three-dimensional setting, the second moment tensor **C** has three eigenvalues, λ_j, and eigenvectors, $\mathbf{v_j}$. By construction:

$$\lambda_1 \geq \lambda_2 \geq \lambda_3 \ . \quad (2)$$

The values of λ_3 and $\mathbf{v_3}$ are key to subsequent analysis. If $\lambda_1 \approx \lambda_2 >> \lambda_{3,}$ the edge attribute defines a plane that is normal to the third eigenvector, $\mathbf{v_3}$. . If $\lambda_1 \approx \lambda_2 \approx \lambda_3$ then the coherence data represents either chaotic (λ_3 large) or homogeneous (λ_3 small) seismic facies. In such cases, the orientation of the geological feature becomes randomized and does not represent a planar discontinuity. The eigenvectors $\mathbf{v_1}$ and $\mathbf{v_2}$ define a plane that

least-squares fits the cloud of edge attributes, α_m. Figure 1 shows a cartoon of the analysis window used to calculate the attribute enhancement.

In order to display the orientation of a planar feature, I define the "fault" dip magnitude, θ, to be

$$\theta = \text{ACOS}(v_{33}), \tag{3}$$

and the "fault" dip azimuth, to be

$$\psi = ATAN(v_{32}, v_{31}), \tag{4}$$

with the three components of eigenvector $\mathbf{v_3}$ defined as

$$\mathbf{v_3} \equiv \hat{\mathbf{x}}_1 v_{31} + \hat{\mathbf{x}}_2 v_{32} + \hat{\mathbf{x}}_3 v_{33} \tag{5}$$

where the x_1-axis is oriented positive to the North, the x_2-axis positive to the East, and the x_3-axis positive down. Here I use the word "fault" in quotes; while I am interested in mapping and enhancing faults, this method works similarly for mapping any discontinuity, such as angular unconformities. If the input attributes α_m were most positive curvature, I would sharpen fold axes. The word "fault" will help me differentiate these dips from those of the reflector's dip-magnitude and dip-azimuth that I will discuss later. Using a multiattribute display technique described by Marfurt (2015), I plot fault dip-azimuth against a cyclical color bar, fault dip-magnitude against a monochrome gray scale, and the fault probability against a monochrome white scale (Figure 2). Note in this image that the fault dip-azimuth ranges between -180^0 and $+180^0$. Thus a near vertical fault dipping towards the southwest may be described by ($\theta=80^0$, $\psi=-120^0$) and appears as green, while one dipping to the northeast may be described by ($\theta=80^0$, $\psi=+60^0$) and appears as magenta. The accuracy of the fault dip magnitude depends on the accuracy of the time-depth conversion described earlier. This

color mapping results in horizontal features such as unconformities appearing as monochrome gray.

Fault smoothing and edge enhancement using the directional Laplacian of a Gaussian operator

Laplacian operators are commonly used in sharpening photographic images (Millan and Valencia, 2005). Unfortunately, such sharpening can exacerbate short wavelength noise. In contrast, Gaussian operators are used to smooth such images. The "Laplacian of a Gaussian" or LoG operator avoids some of the artifacts of the Laplacian operator itself by smoothing high frequency artifacts prior to sharpening. Using the associative law when creating the operator, one finds that

$$\mathbf{L}\left(\mathbf{G}\boldsymbol{\alpha}\right) = \left(\mathbf{LG}\right)\boldsymbol{\alpha}. \tag{6}$$

The composite LoG operator will have the general form:

$$\mathbf{LG}\,\boldsymbol{\alpha} = -\sum_{m=1}^{M} \frac{1}{\pi\sigma^4}\left(1 - \frac{x_{1m}^2 + x_{2m}^2 + x_{3m}^2}{3\sigma^2}\right)\exp\left(-\frac{x_{1m}^2 + x_{2m}^2 + x_{3m}^2}{2\sigma^2}\right)\alpha_m\,, \tag{7}$$

where σ^2 defines the variance of the Gaussian smoother.

Such a mathematical implementation has two advantages. First, one can precompute the LoG operator, rather than cascade two separate operations, resulting in a more efficient algorithm. Second, one is no longer restricted to orienting the Laplacian operator along the seismic acquisition axes, allowing one to implement a directional filter.

Directional smoothing and sharpening

I modify the dLoG operator to be directional, smoothing along the direction perpendicular to the planar discontinuity defined by the eigenvectors $\mathbf{v_1}$ and $\mathbf{v_2}$. I define the Gaussian to be elongated along the planar axes:

$$G_{mn} = exp\left[-\frac{\mathbf{1}}{\mathbf{2}}\boldsymbol{x'^{T}_{m}\Sigma^{-1}x'_{n}}\right], \tag{8}$$

where $\mathbf{\Sigma}$ is defined as:

$$\boldsymbol{\Sigma} = \begin{pmatrix} \sigma_1^2 & 0 & 0 \\ 0 & \sigma_2^2 & 0 \\ 0 & 0 & \sigma_3^2 \end{pmatrix}, \tag{9}$$

And where $\sigma_1 = \sigma_2 = 3\sigma_3$, and where **x**' indicates the coordinates of the voxels in the analysis window within the rotated coordinate system, aligned with the hypothesized fault. In my examples, the bin size Δy = 25m, Δx = 12.5m; to have good numerical support of the dLoG I set σ_3 = 25 m and $\sigma_1 = \sigma_2$ = 75 m. In my original (unprimed system), the Gaussian then becomes:

$$G_{mn} = exp[-\boldsymbol{x_m^T R^T \Sigma^{-1} R x_n}], \tag{10}$$

where **R** is the rotation matrix that aligns the new **x'**-axis with $\mathbf{v_3}$ given by:

$$\mathbf{R} = \begin{pmatrix} v_{11} & v_{21} & v_{31} \\ v_{12} & v_{22} & v_{32} \\ v_{13} & v_{23} & v_{33} \end{pmatrix}. \tag{11}$$

The second derivative of the Gaussian in the $\mathbf{x_3}$'direction can be written as:

$$\frac{d^2G}{dx'^2_3} = \gamma\left[\frac{-2}{\lambda_3} + 4x'^2_3\right]\exp\left[-\frac{1}{2}\left(\frac{x'^2_1}{\sigma_1^2} + \frac{x'^2_2}{\sigma_2^2} + \frac{x'^2_3}{\sigma_3^2}\right)\right], \tag{12}$$

where γ represents a normalization term.

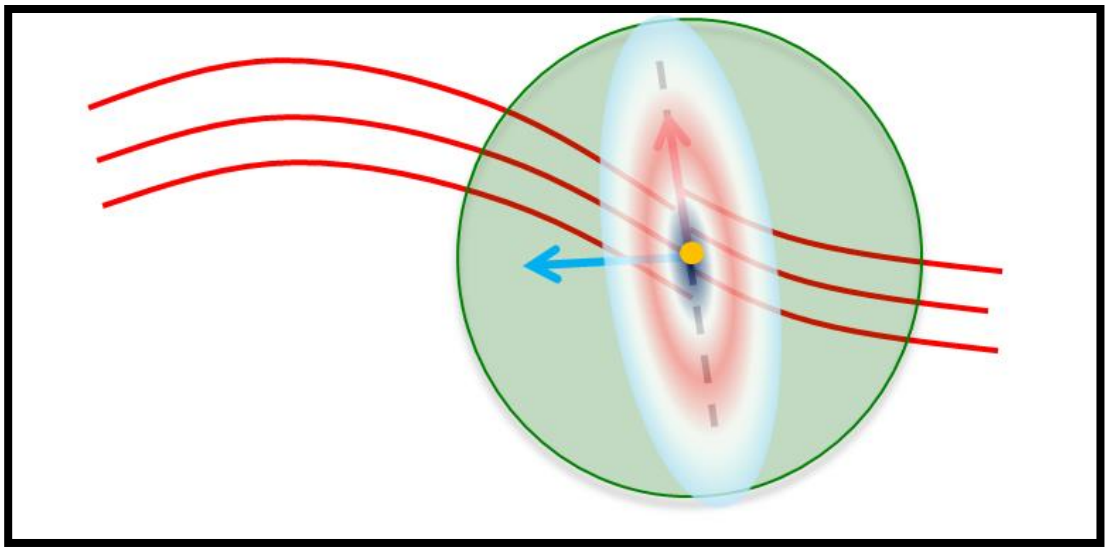

Figure 1. Cartoon showing reflectors (as solid red lines) and a coherence anomaly (as black dotted line). The analysis window (in green) is a circle centered on the analysis point (in orange). The eigenvector $\mathbf{v_3}$ is perpendicular to the fault plane reflector (blue arrow), while the normal vector **n** is perpendicular to the reflector (red arrow). The dLoG operator (red negative and blue positive) is short in the direction parallel to $\mathbf{v_3}$ and three times longer in the direction parallel to $\mathbf{v_1}$ and $\mathbf{v_2}$

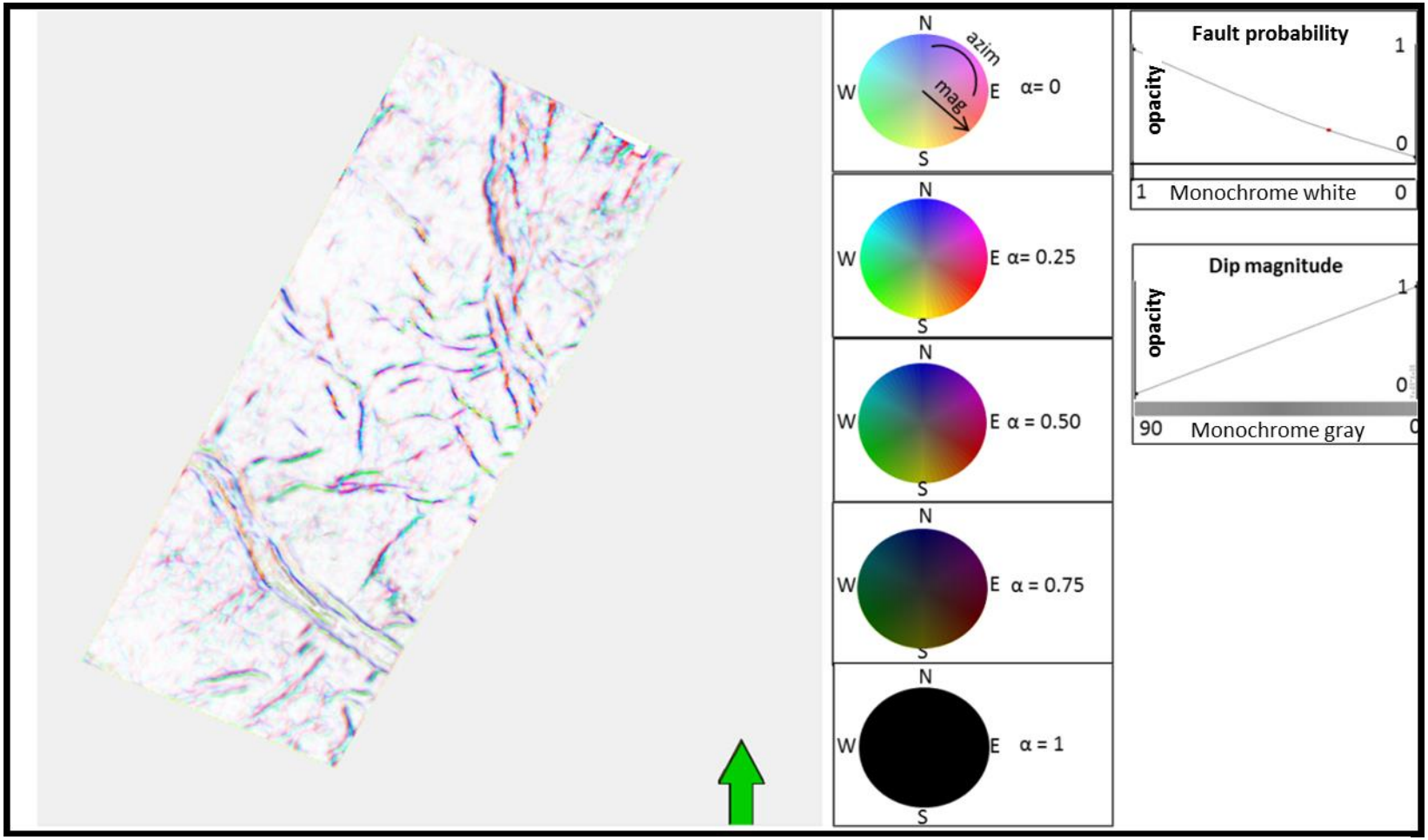

Figure 2. Time slice at t= 2.52 s through co-rendered fault dip-azimuth, fault dip-magnitude and LoG filtered coherence (fault probability). The fault probability is plotted against lightness, with low values opaque (white) and high values transparent.

Chapter 2: dLoG application on two New Zealand basins

The next section was also published in Machado et al (2016).

I evaluate my proposed algorithm by applying it to two seismic volumes from offshore New Zealand. The first survey is over the Great South Basin (GSB) that lies off the southeast coast of the South Island of New Zealand. The basin formed during the mid-Cretaceous and is divided into several highly faulted sub-basins. The second survey is from the Canterbury Basin of the eastern coast of South Island, New Zealand. A geologic summary is provided in the Appendix.

Great South Basin

Figure 3 shows a time slice and a vertical slice through the GSB seismic amplitude volume. Figure 4 shows the same slices through the corresponding coherence volume computed along structural dip. Note the fault pattern in the central part of the survey, seen on both amplitude and coherence slices. Other coherence anomalies are noticeable at t=1.35 s on the vertical slice indicating a series of steeply dipping faults.

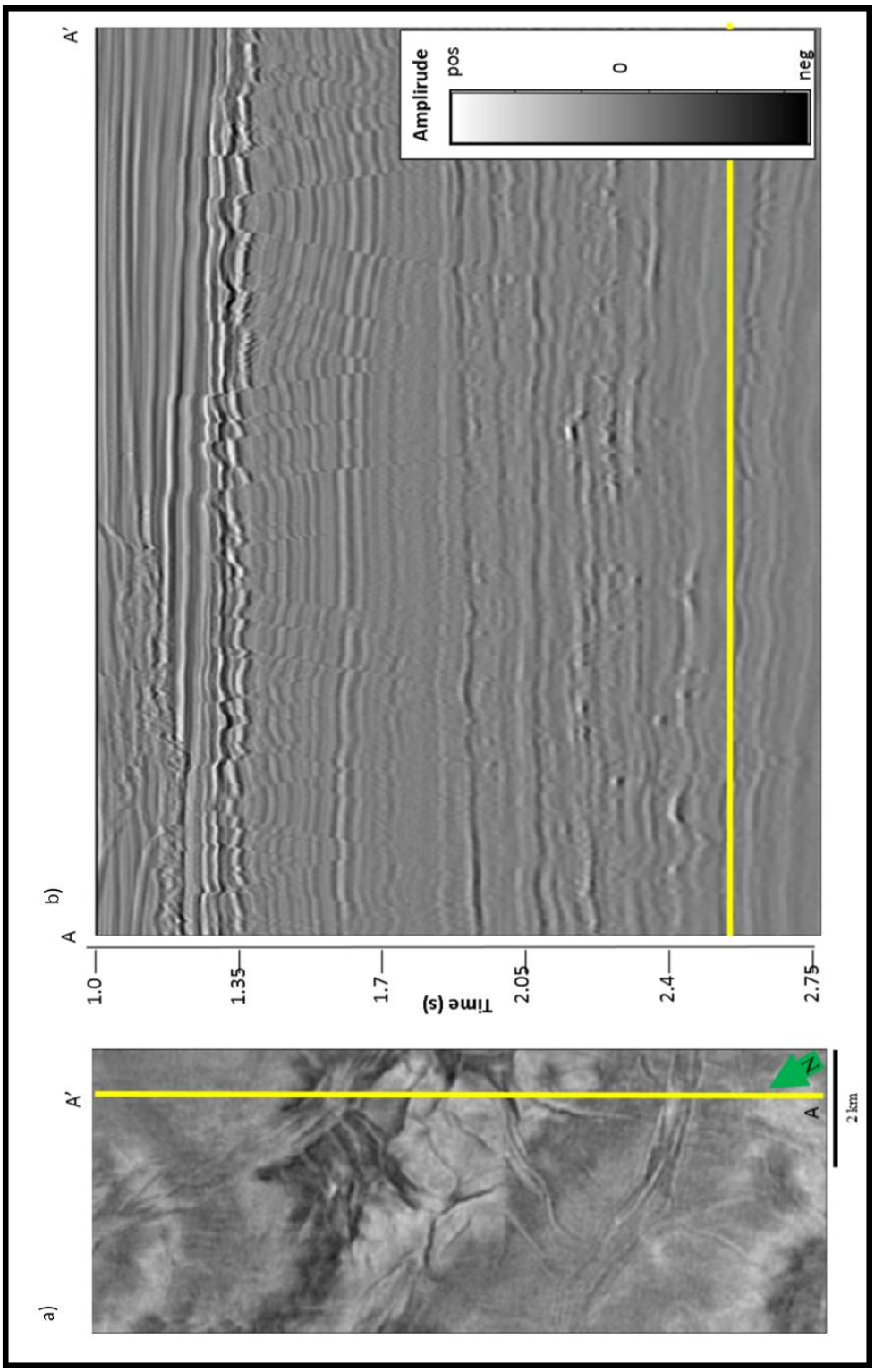

Figure 3. (a) Time slice at t=2.52 s and (b) vertical slice along AA' through a seismic amplitude volume with a bin size of 12.5 by 25 m.

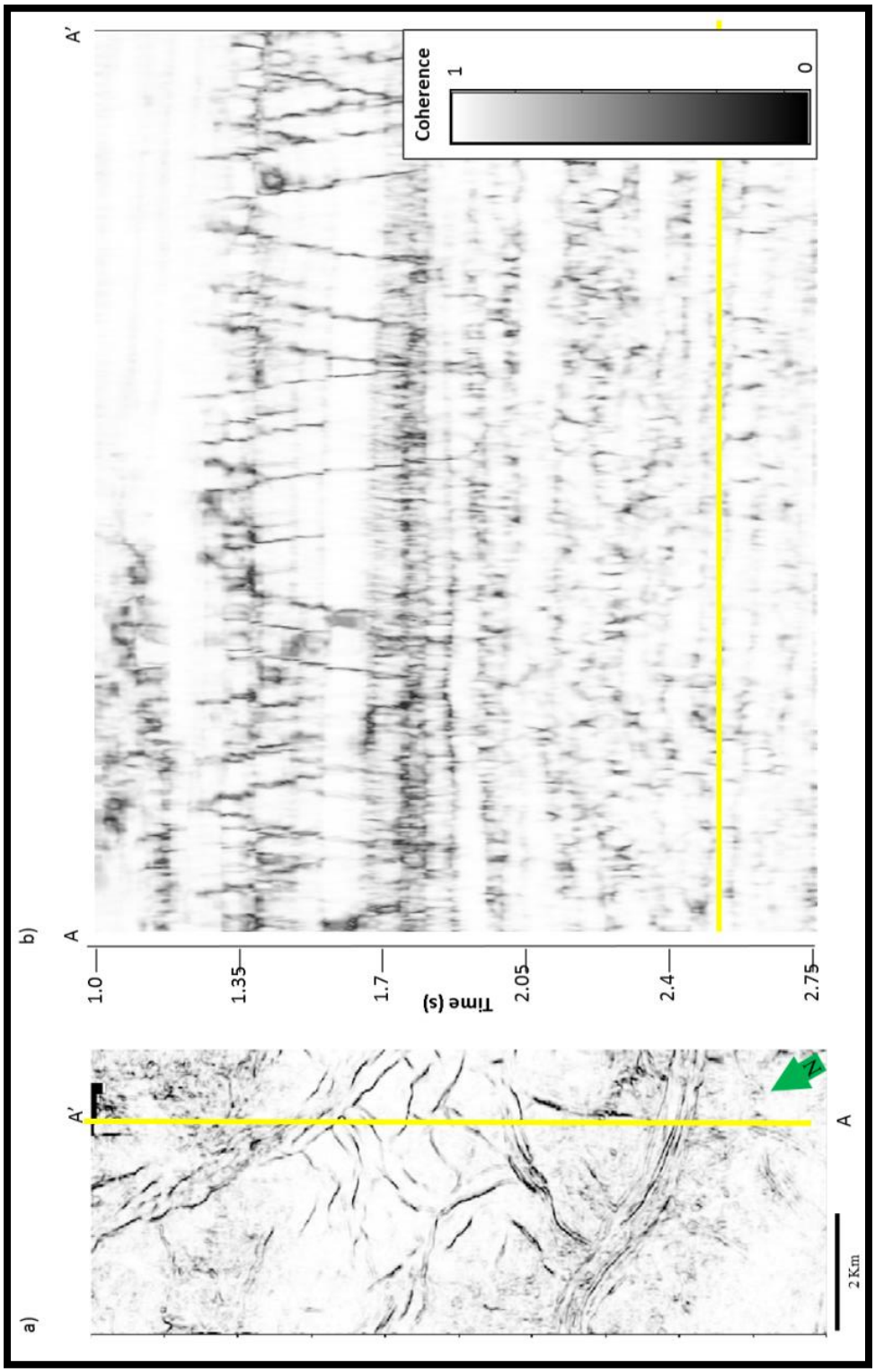

Figure 4. (a) Time slice at *t*=2.52 s and (b) vertical slice along AA' through a coherence volume computed from the seismic amplitude data shown in Figure 3. The orientation of the coherence anomalies in (a) are shown on Figure 2.

I now sharpen the image shown in Figure 4 through the application of the dLoG operator and display the results in Figure 5. Using a conversion velocity of 3000 m/s and a 75 m radius analysis window the directional LoG filter sharpens the fault features and removes high frequency noise from the input coherence volume. In addition to sharpening, I apply a filter (Figure 5c) that suppresses coherence anomalies parallel to reflector dip. Fault features indicated by block arrows are more prominent and easier to pick while some of the noise is suppressed. The conversion velocity was the same as that used to compute reflector dip and azimuth.

Note that the dLoG filter followed by a dip magnitude filter enhances the faults at t=1.35 s in the upper portion of the vertical cross-section and improved its continuity.

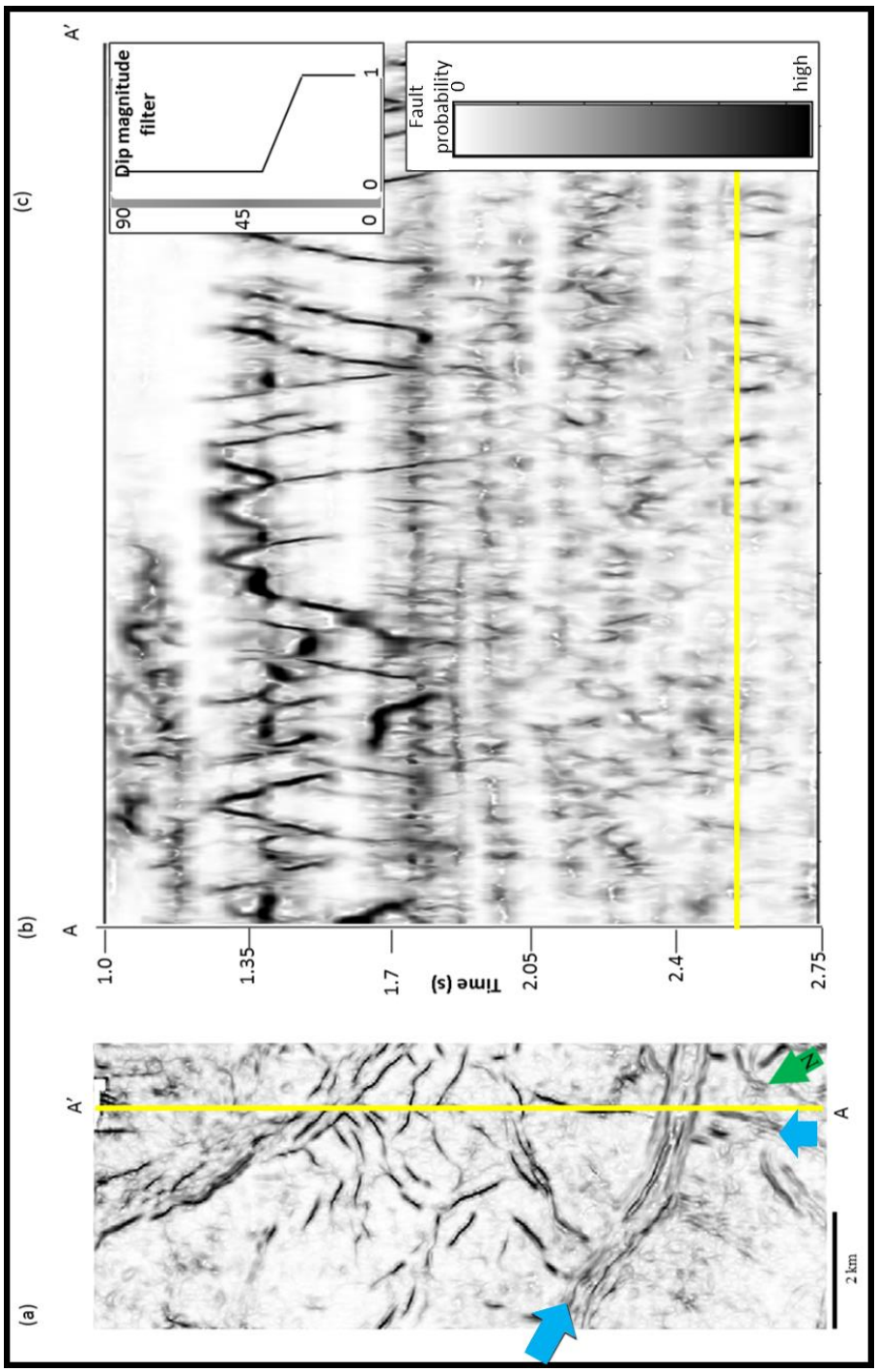

Figure 5. (a) Time slice at *t*=2.52 s and (b) vertical slice along AA' through the directional dLoG attribute computed from the coherence volume shown in Figure 5. (c) Filter applied to coherence computed from the dip magnitude of $\mathbf{v_3}$ that suppresses features parallel to reflector dip. Block blue arrows indicate faults that are now more continuous and easier to identify.

Figure 6 shows the components of eigenvector $\mathbf{v_3}$ co-rendered with the directional dLoG fault probability volume. The fault or unconformity dip–magnitude with respect to the reflector of any given planar event is defined by v_{33}. I plot this attribute against saturation in an HLS display. The azimuth, ψ, of steeply dipping planar events (typically faults) is computed from equation 4, where axis 1 is North. Fault probability values are plotted against transparency such that high fault probability events appear to be transparent on an otherwise white background.

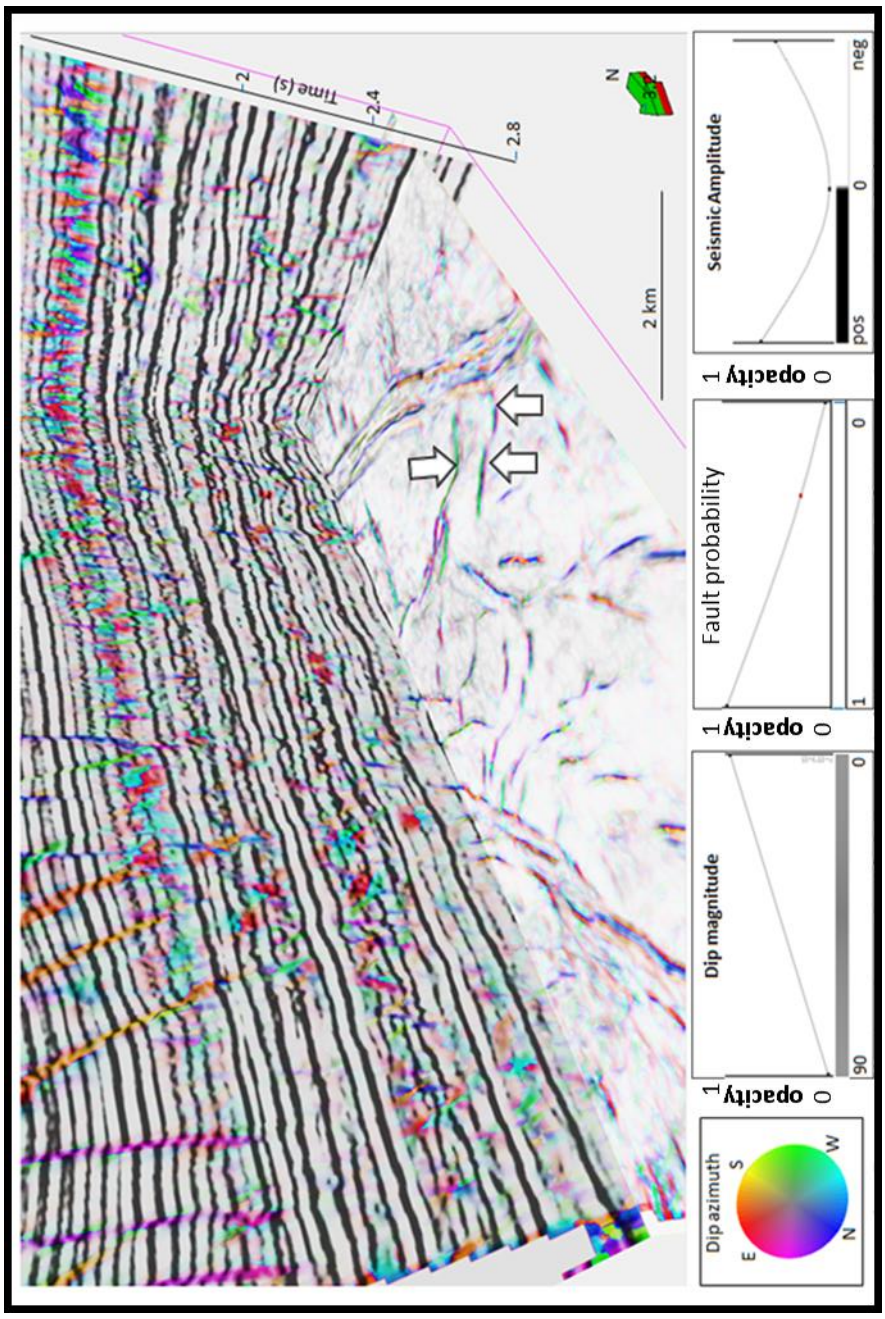

Figure 6. Time slice at *t*=2.52 s through co-rendered fault dip-azimuth, fault dip-magnitude, fault probability and seismic amplitude. The fault dip magnitude and azimuth are computed from v_3. The opacity used for each attribute is displayed on top of the color bar. Fault dip azimuth is plotted against a cyclical color bar, fault dip magnitude against a monochrome gray scale, the dLoG attribute against a monochrome white scale and seismic amplitude against a black and white binary color bar. Fault dip azimuth and magnitude can be easily characterized through this combination of attributes. Sharpened events sub parallel to the vertical slices appear smeared (blue and yellow on the N-S line, red and green on the E-W line).

Figure 6 clearly exhibits the orientation of the fault systems present in the data. The southern faults on the time slice show a predominant southwest dipping direction (green), while in the northern region I can see an eastward dipping direction. On most of the faults, I can see a nearly parallel fault of opposite azimuth, representing the fundamental motion of faults defining horsts and grabens appearing as green/pink (west/east) and the blue/yellow (north/south) linear couplets. On the vertical slices, the orientation of the fault azimuth is more clearly seen. Faults sub parallel to the vertical slice appear "blurred". Notice the northward-dipping faults in the upper left portion of the image, with the events clearly shown in the overlaid seismic amplitude.

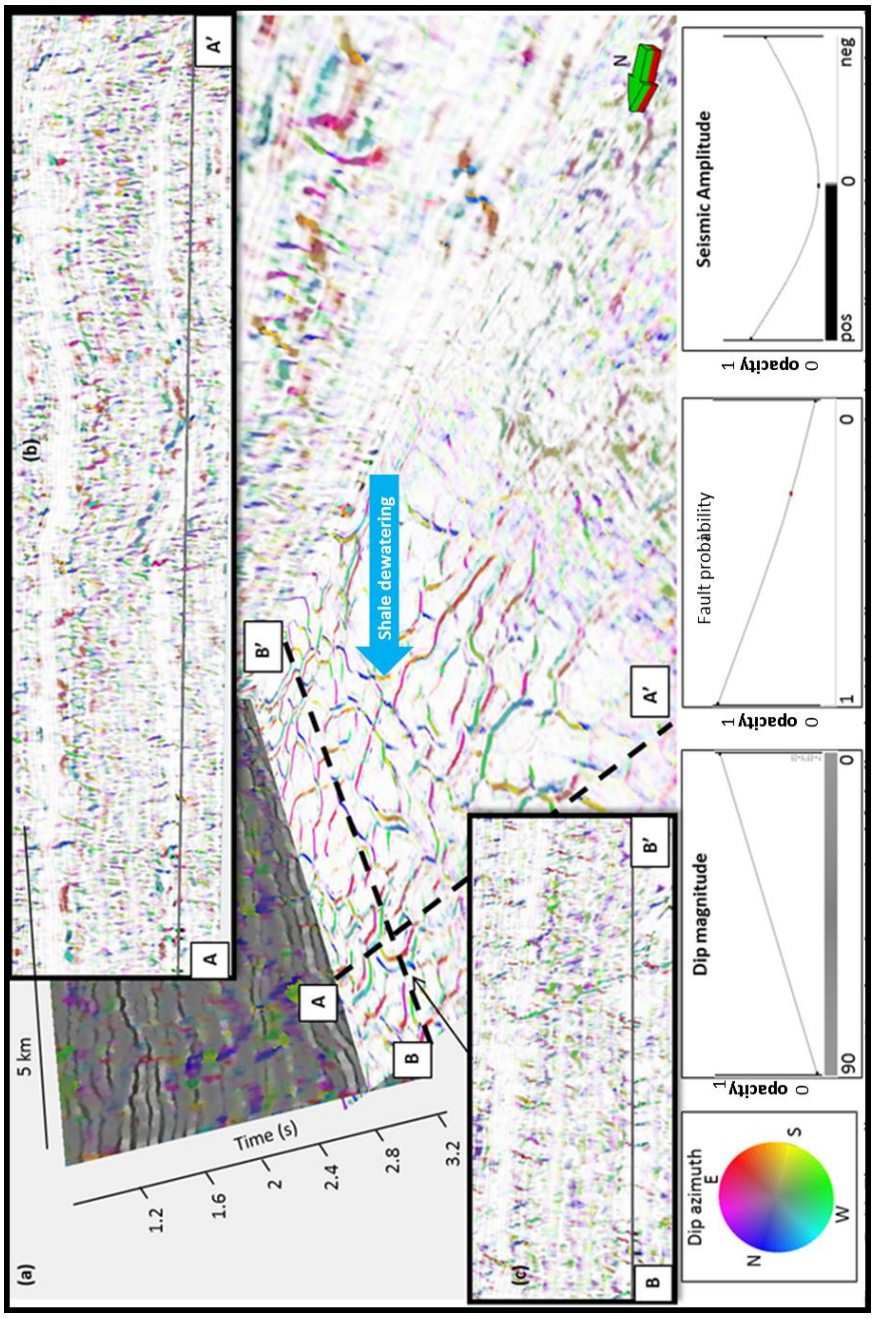

Figure 7. (a) Time slice at t= 2.8 s through co-rendered fault dip-azimuth, fault dip-magnitude, fault probability and seismic amplitude. The fault dip magnitude and azimuth are computed from $\mathbf{v}_3$. The opacity used for each attribute is displayed on top of the color bar. Fault dip azimuth is plotted against a cyclical color bar, fault dip magnitude against monochrome gray the fault probability attribute against monochrome white and seismic amplitude against a black and white dipole color bar. Shale dewatering features are pointed with the blue block arrow. (b) and (c) show two vertical lines with orthogonal orientation and the seismic image of the shale dewatering features with an outward dipping trend.

The dip magnitude of the fault features is also displayed on Figure 6. Notice how the southern fault system (right side of the image) is less bright than the northern one, which indicates that it is less vertical. Most of the horizontal events were suppressed by the application of the filter shown in Figure 5c.

Canterbury Basin

Figure 7 shows a seismic image of shale dewatering features from the Canterbury Basin survey acquired in New Zealand. The directional Laplacian of a Gaussian highlights and sharpens the linear features, while the eigenvectors represent their azimuth and dip magnitude. Examination of the polygonal fault system highlighted shows an outward-dipping trend for most of the features.

Figure 8 shows seismic images of a turbidity system in the Canterbury Basin survey before and after directional dLoG filtering of coherence. The coherence image in Figure 8a shows channels in the central and northeastern portion of the image. Figure 8b after dLoG and dip magnitude filtering shows an image that is noticeably cleaner, with discontinuities more sharply defined. Finally, Figure 8c shows the steeply dipping edge channels through the "fault" dip-magnitude and dip-azimuth. Notice how the northern edge of the channels of the central portion of the image is dipping northward. This can also provide information on the nature and depositional direction of the sediments.

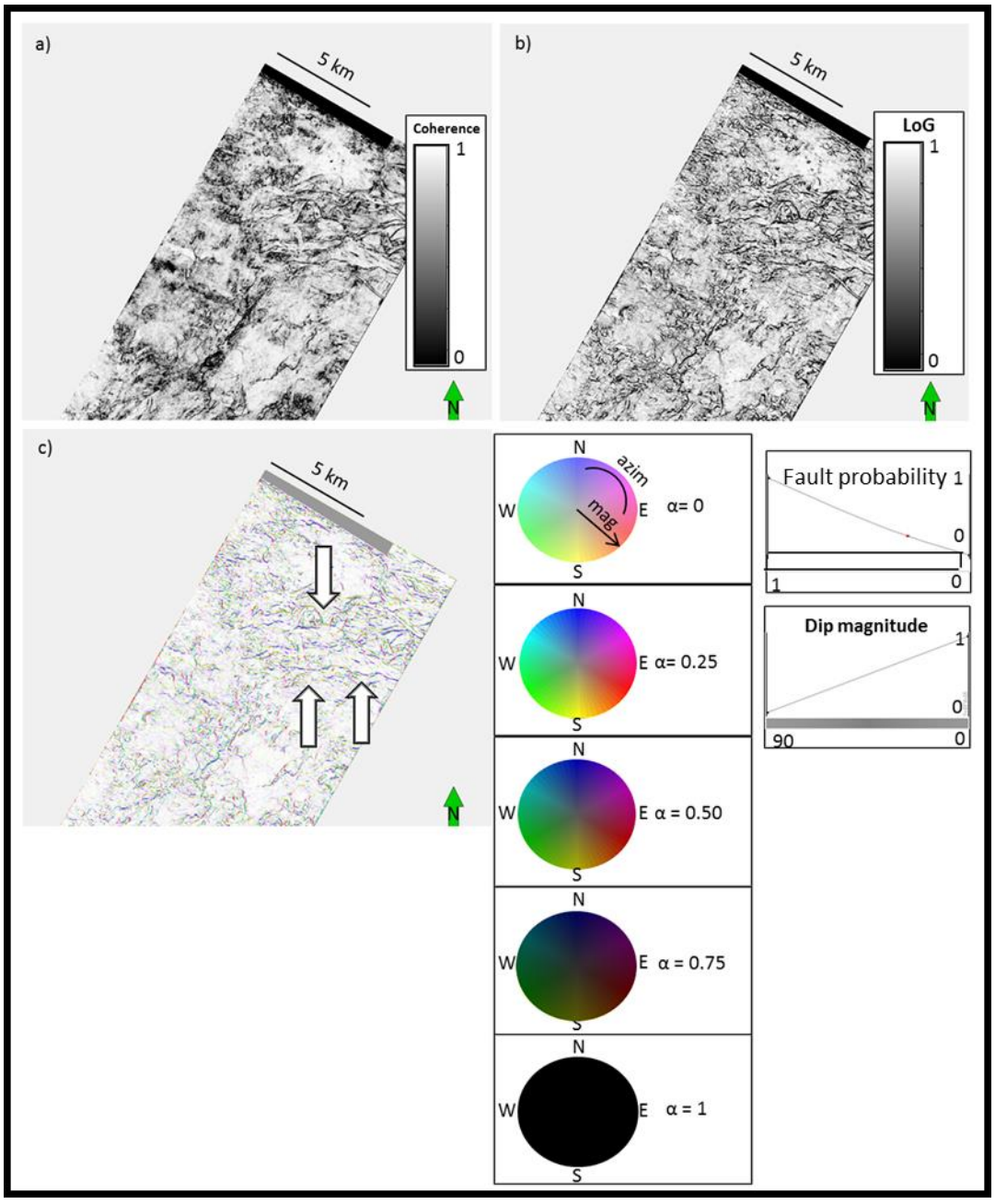

Figure 8. Time slice at *t*=2.04 s through a) coherence, b) dLoG of coherence fault probability c) co-rendered fault dip-azimuth, fault dip-magnitude and dLoG of coherence ("fault" probability). The fault dip magnitude and azimuth are computed from $\mathbf{v}_3$. The transparency function used for each attribute is displayed on top of the color bar. Fault dip azimuth is plotted against a cyclical color bar, fault dip magnitude against a monochrome gray color bar, fault probability against a monochrome white color bar. Channel features are easily recognized through the conventional coherence, but sharpened and cleaner after dLoG filtering. The channel edges are further characterized by combining with fault dip magnitude and azimuth attributes.

Figures 5-8 showed images generated using the dip magnitude filter described in Figure 5c. Similar filters can be designed on either dip-azimuth. Figures 9 and 10 show two different tapers applied to the same dataset at the same depth as the one shown on Figure 6. In Figure 9, I enhance low coherence events parallel to structural dip, and reject discontinuities with a dip greater than 25°. Such features appear grayer since the reflectors are relatively flat.

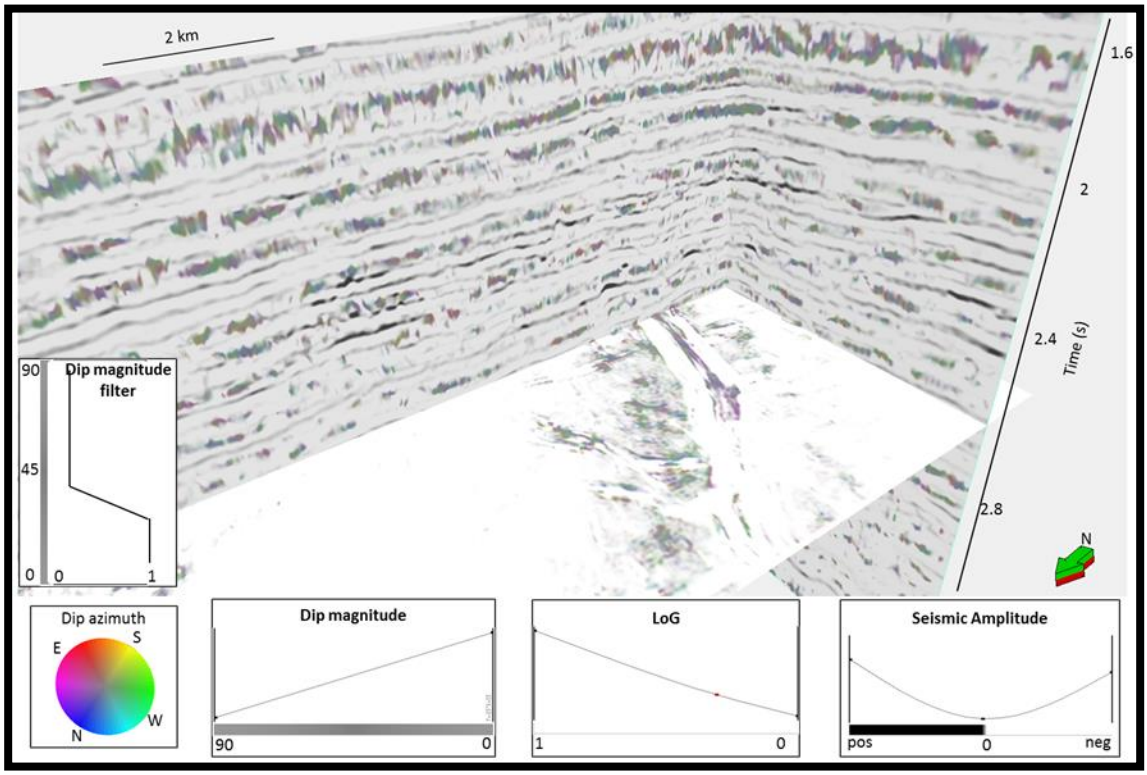

Figure 9. Time slice at *t*= 2.52 s through faults shown in Figure 6 highlighting near horizontal discontinuities through the use of a taper which hinders any feature with a dip greater than 25°.

In contrast, Figure 10 shows the same slices as in Figure 9 but with a filter that rejected features with a dip magnitude less than 65°. The faults are brighter since they are steeper with less of a gray overprint in the display. The faults in the central part of the survey are more steeply dipping while those to the north have been filtered out.

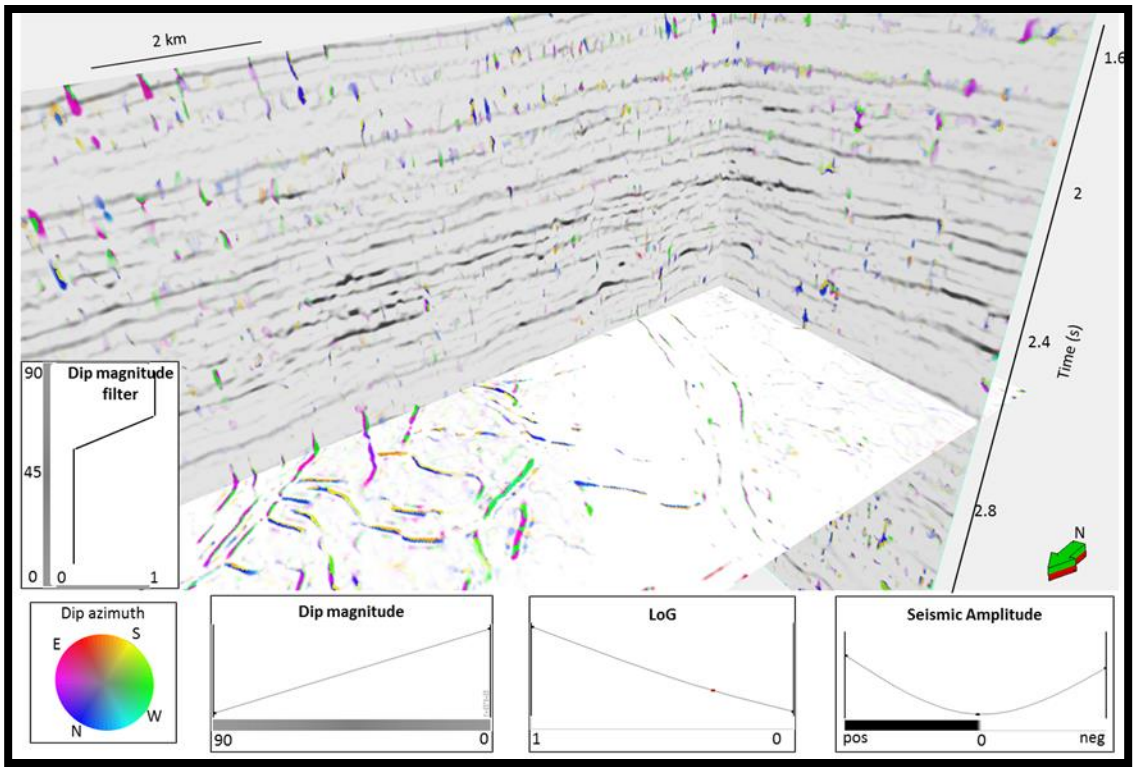

Figure 10. Time slice at *t*= 2.52 s through faults corresponding to Figure 6 with a dip magnitude filter that reflects features whose dip is less than 65°.

In Figure 11, a box probe was created to isolate and show the 3D image of the polygonal fault system from the Canterbury Basin dataset. Through co-rendered fault dip-azimuth and dip-magnitude, with opacity modulated by the dLoG fault probability attribute, I was able to generate a 3D image of the fault planes. Outward dipping trends can be seen, especially on the right side of the image.

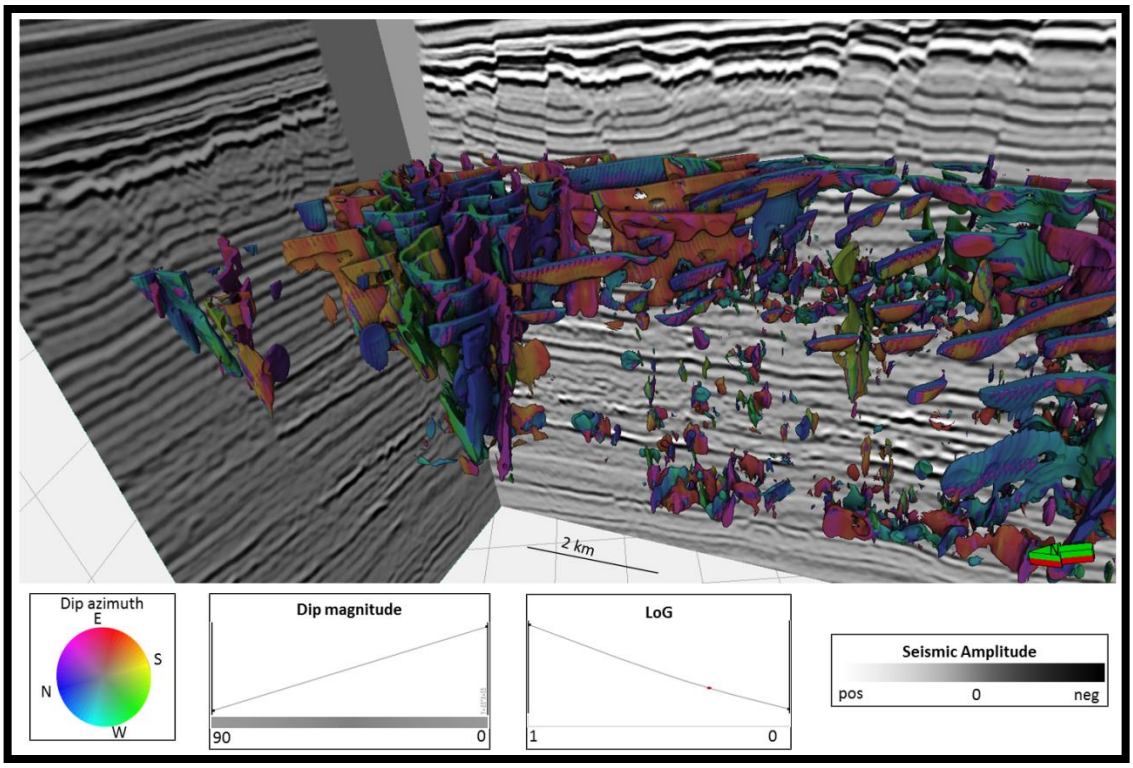

Figure 11. 3D view of two vertical lines through the seismic amplitude volume, and a box probe through co-rendered fault dip azimuth and fault dip magnitude showing polygonal faulting. The fault probability modulates the opacity, where vowels with $\alpha<0.5$ are being rendered transparent. Lineaments that are less than 25° of dip to the reflector have been filtered out.

Figure 12 shows the same box probe as Figure 11. By making use of the same co-rendering parameters I am able to isolate faulting features within a limited range of azimuth. Such manipulation of the dip azimuth of these features allows me to highlight antithetic faulting in the basin, as shown by the opposed dipping directions of the faults portrayed.

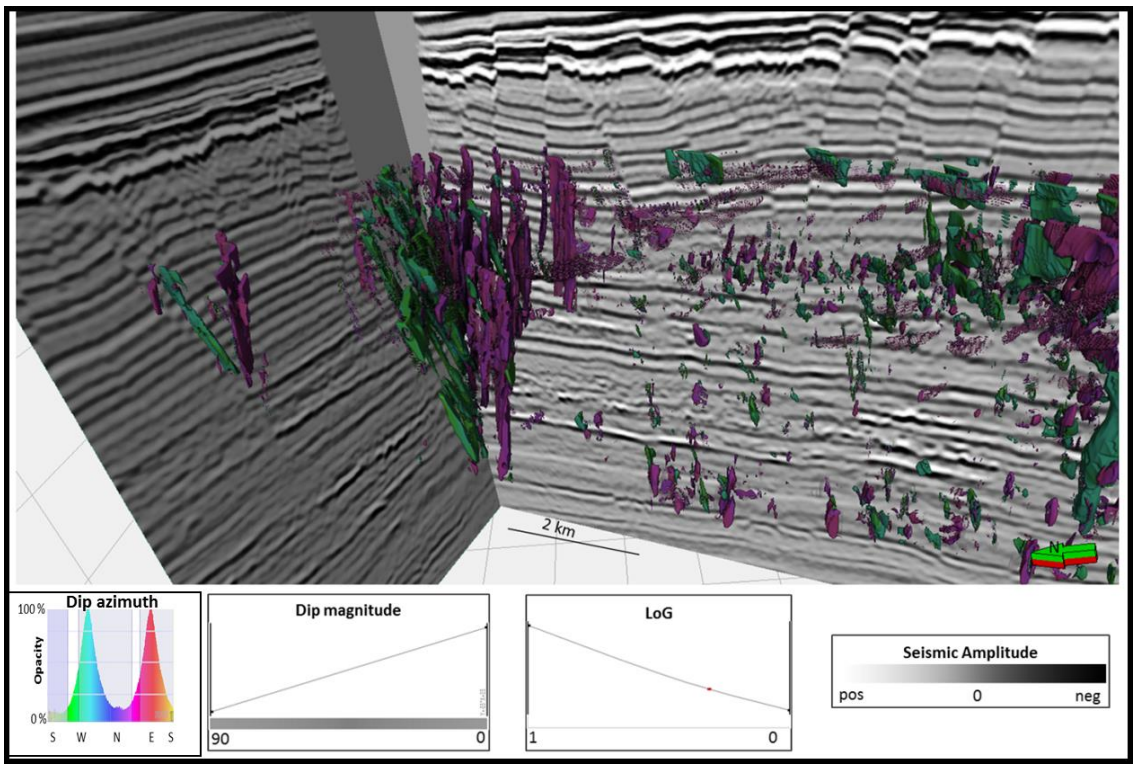

Figure 12. The same image as Figure 11, but now with faults with N and S azimuths rendered transparent. Thus a synthetic and antithetic fault system is highlighted

Chapter 3: dLoG as a preconditioner for ant-tracking and automatic fault picking

Fault picking is a human intensive labor involved in every aspect of any oil and gas exploration and production endeavor. In resource plays faults can be geologic hazard to avoid, while in conventional plays they may also form traps for potential hydrocarbons accumulation. Because many surveys have dozens or even hundreds of faults to be selected and analyzed for interpretation, different approaches have been proposed to solve this problem. One such approach is the ant-tracking algorithm. I used a commercial implementation of ant-tracking with and without the dLoG attribute to evaluate the automatic fault extraction process for a dataset from the New Zealand Taranaki basin.

The ant-tracking algorithm

Ant tracking is an algorithm inspired by the collective foraging behavior of a real ant colony in the nature (Zhao et al., 2015). The concept was first introduced by in the nineties by Colorni et al. (1991) and Dorigo et al. (1997) but only recently has it been adopted by different software platforms as a mean to guide the automatic fault extraction process. Figure 13, taken from Dorigo et al. (1997), explains the concept behind the ant tracking quite well. First ants are randomly sprinkled on a grid point after which they take one of several allowed pathways. Each ant can proceed a fixed number of steps. If the ant finds food it can go further. If not, it dies. Each deposits pheromones as it travels and more ants come that way. In this manner, the shorter paths with more food will be populated with the most ants

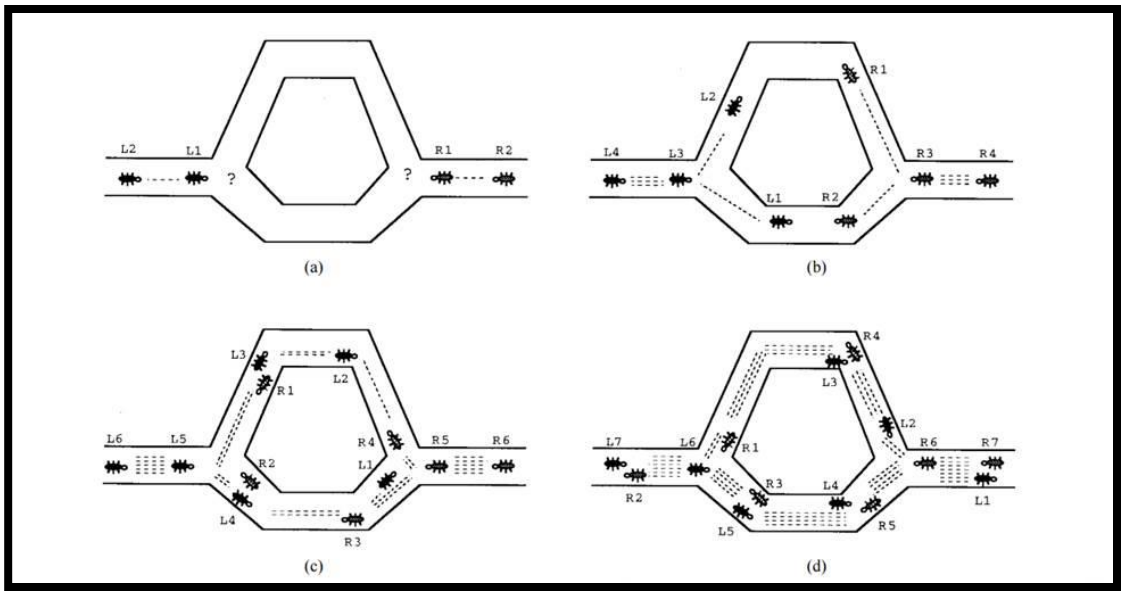

Figure 13. A model of how real ants find the shortest path. (a) Ants arrive at a decision point. (b) Some ants choose the upper path and some the lower path. The choice is random. (c) Since the ants move at approximately a constant speed, the ants that choose the lower, shorter, path reach the opposite decision point faster than those that choose the upper, longer, path. (d) Pheromone accumulates at a higher rate on the shorter path due to a higher amount of ants crossing it. The number of dashed lines is approximately proportional to the amount of pheromone deposited by ants (taken from Dorigo et al., 1997).

This concept of swarm intelligence may be applied to geological problems. The idea is to distribute a large number of agents (ants) into a volume so that they move along fault surfaces highlighted by some edge enhancement attribute, such as coherence. Where there are grid points that do not fulfill the conditions for a fault, such as a continuous seismic reflector surface, agents will be terminated shortly (Iske et al., 2005). Figure 14 from Iske et al., (2005) illustrates how the ant-tracking algorithm helps to delineate fault and discontinuities while rejecting noise.

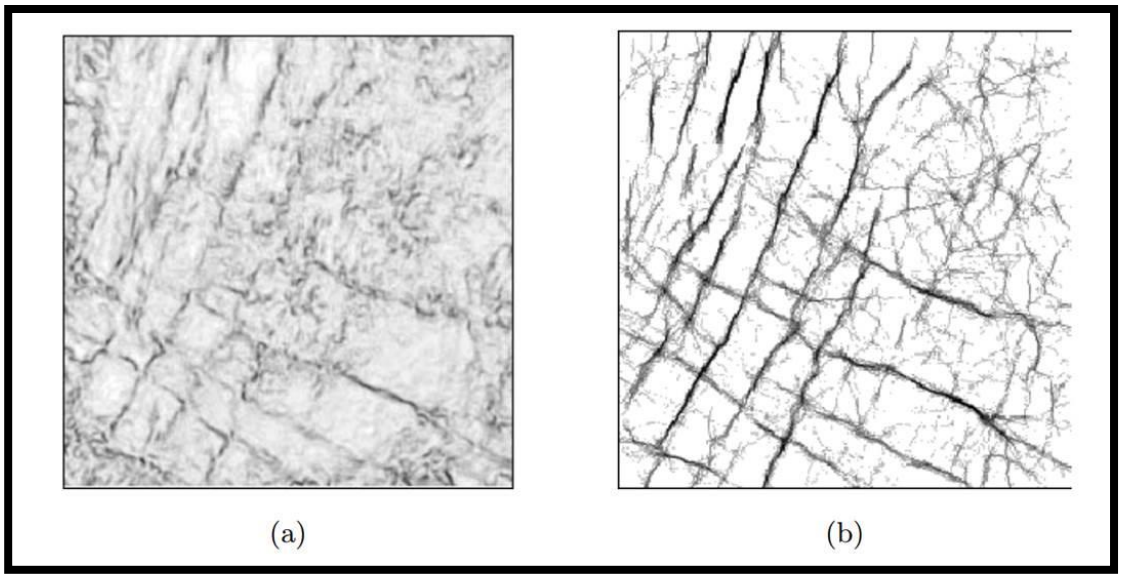

Figure 14. (a) Time slice through a fault attribute (variance) with (b) corresponding ant tracking results (after Iske et al., 2005).

Figure 15 shows a vertical slice through a seismic amplitude volume acquired over the Taranaki Basin, New Zealand. Note the relatively flat geology for the first second of seismic data, followed by an unconformity, which is inferred to be an incised valley. The next part of the seismic section is highly faulted.

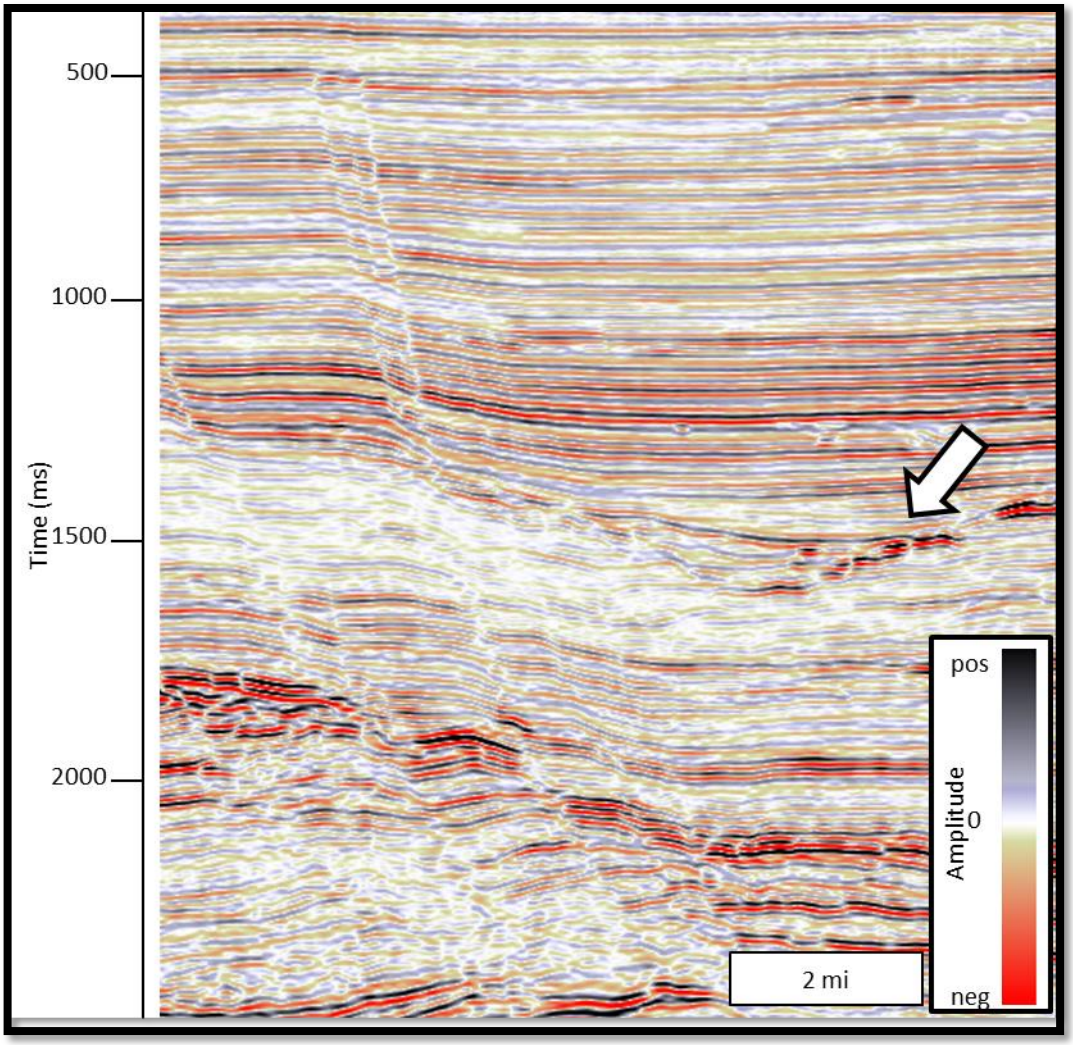

Figure 15. Seismic amplitude of survey from the Taranaki Basin. Relatively flat geology on top of normally faulted sequences below 1500 ms. Block arrow indicates an unconformity.

Figures 16 through 19 show the same cross section shown on Figure 15 through three different edge enhancement attributes. Each attribute was used as input to generate an ant-tracking attribute for subsequent automatic fault extraction.

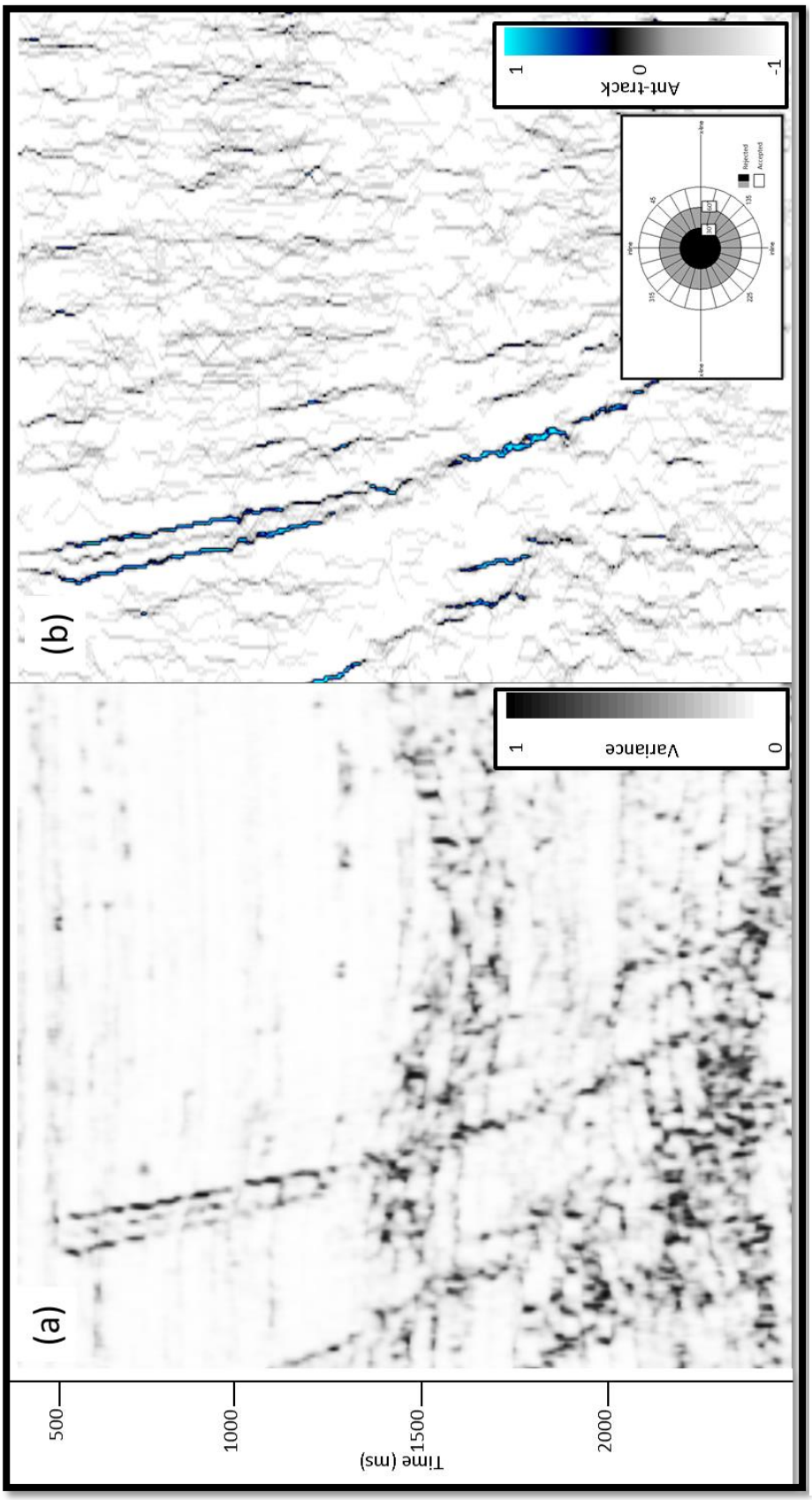

Figure 16. The same vertical section from Figure 15 through (a) variance attribute and (b) corresponding ant-tracked attribute. The stereonet shows that ants were constrained to search within a cone of 30° about the vertical (fault dips > 60°).

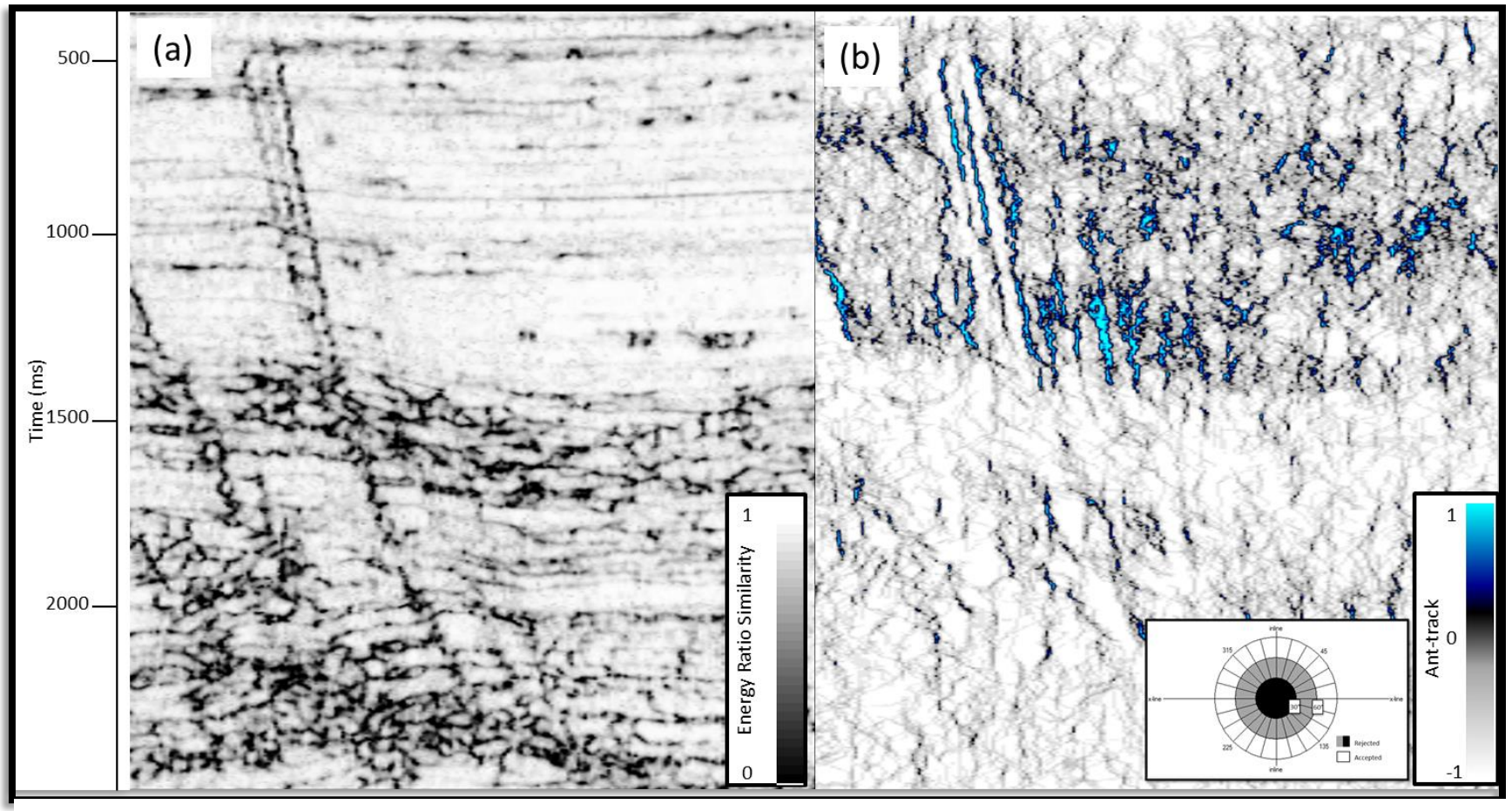

Figure 17. The same vertical slice shown in Figure 15 through (a) Energy Ratio Similarity attribute and (b) corresponding ant-track attribute. Note noise in the upper right region of the right image.

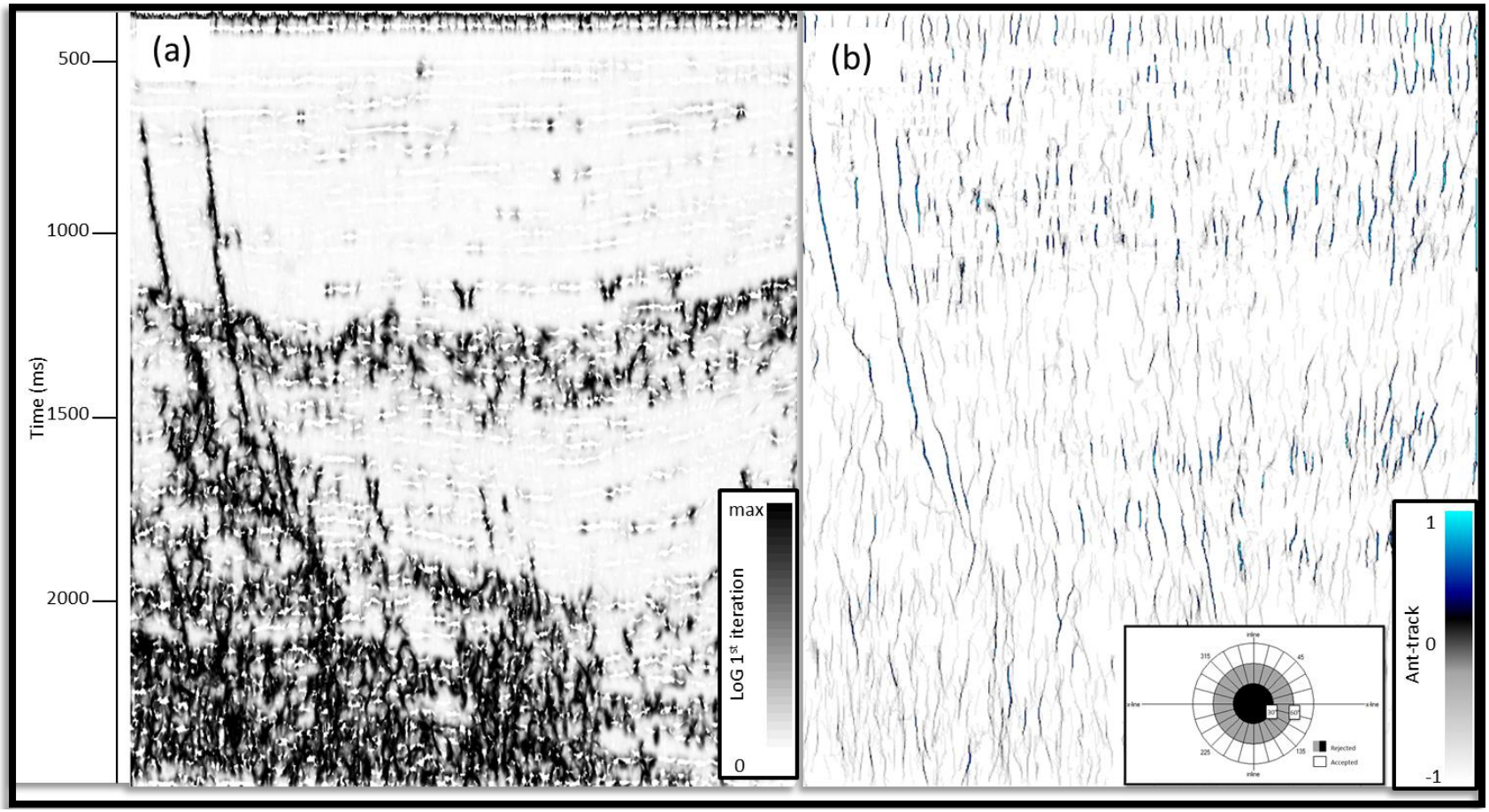

Figure 18. The same vertical slice shown in Figure 15 through (a) first iteration of LoG attribute and (b) corresponding ant-track attribute. Note noise diminishment in the upper right region of the right image.

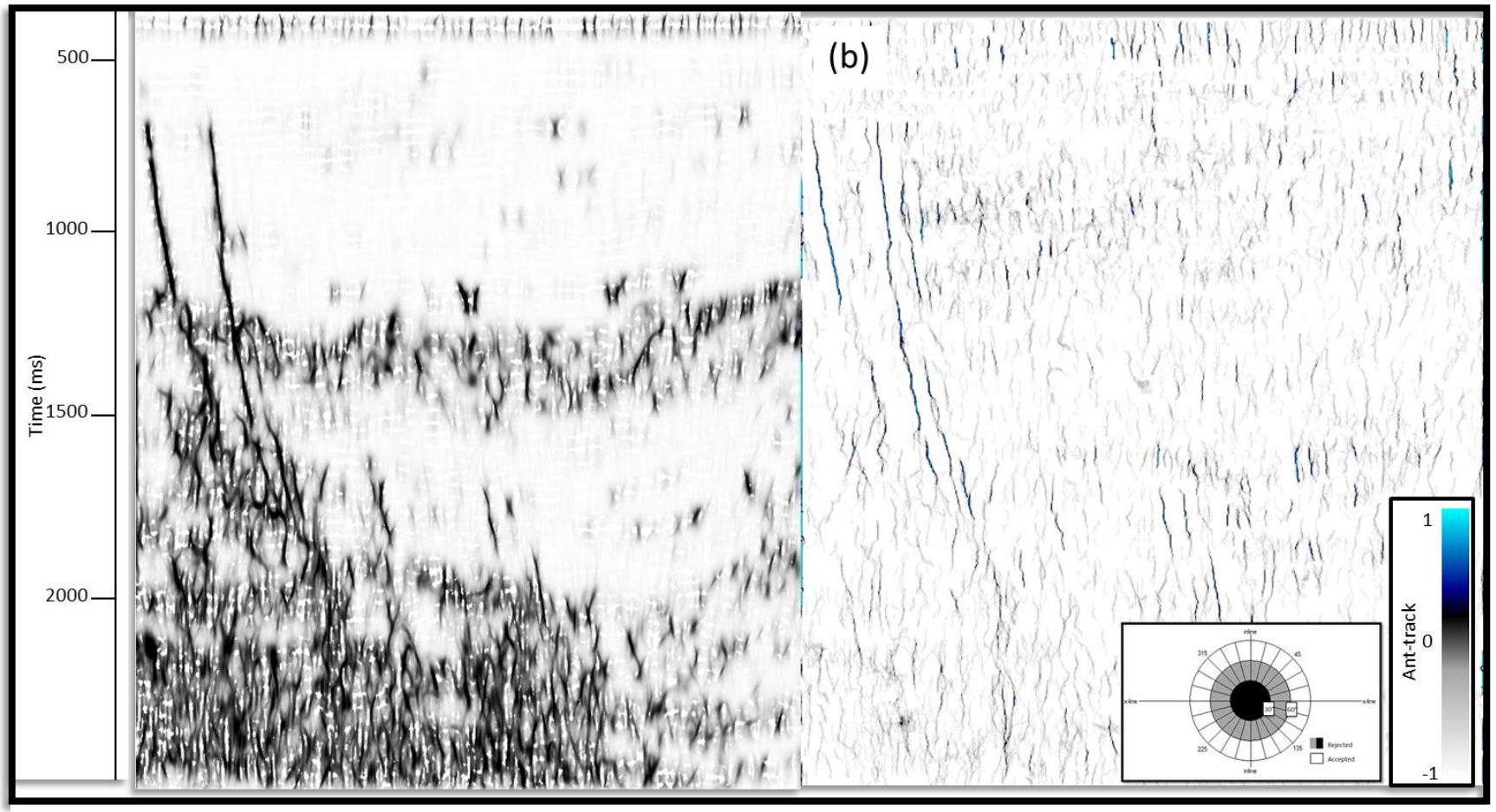

Figure 19. The same vertical slice shown in Figure 15 through (a) fault probability after the third iteration of dLoG filtering and (b) corresponding ant-track attribute. Note noise diminishment in the upper right region of the right image and improved fault resolution.

The variance on Figure 16 does a good job in highlighting discontinuities but is relatively unfocused, which results in a more diffuse ant-track image. Energy ratio similarity (Figure 17) is a measurement of coherence that works very well with highlighting and sharpening discontinuities as faults, but also highlights other types of discontinuities which also affects the corresponding ant-track image. The subtle vertical discontinuities in the upper right portion of the ant-track algorithm will represent a challenge for the later automatic fault extraction.

Figure 18 shows the same vertical slice through the directional Laplacian of a Gaussian fault probability attribute computed iteratively. In the first iteration, I enhance steeply dipping features but suppress features parallel to reflector dip. With these stratigraphic features removed, the second iteration of fault enhancement is better able to link up faults that were previously cut by unconformities and other stratigraphic discontinuities. The third iteration (Figure 19a) reduces noise such that the resulting image looks cleaner and sharper. Furthermore, subsequent ant-tracking (Figure 19b) shows significantly less noise in the upper right portion of the image, which will make the fault extraction process much simpler.

For each one of the ant-tracked attributes shown on Figures 16-19, the parameters were as following:

Table 1 Ant-tracking parameters for edge enhancement attributes

Ant-tracking Parameter	Value
Number of ants	7
Ant track deviation	2
Ant step size	3
Illegal steps allowed	1
Legal steps required	3
Stop criteria	5

The number of ants refers to the ant density the program will be allowed for fault tracking. A higher value means higher density, but also higher computational time. Ant track deviation refers to the amount of illegal steps allowed outside of a delimited fault. The higher this value the more interconnected features will appear in the final result. The ant step size refers to how many voxels or ants per step are allowed, which translates into higher resolution for smaller sizes. Illegal steps allowed are the amount of steps that the algorithm will take outside of a delimited discontinuity. Legal steps required refers to how connected the faults must be in order distinguish edges from noise. The stop criteria value is the percentage of illegal steps allowed before terminating an agents life.

Fault object extraction

With the computed attributes I next evaluate how the different images affect a commercial automatic fault extraction tool. To validate the process, I manually picked three faults from the seismic data, thus generating my control groups. With considerable self-confidence, I assume manually picked faults are the closest approximation to reality. Figure 21 shows a 3D image of the manually picked faults, along a representative amplitude slice from which they were taken. All three faults are prominent in the seismic survey, so they did not represent a big challenge to pick

The workflow for the commercial automatic fault object extraction software requires an edge enhancement attribute as input. The extraction program generates an array of fault patches that follows the discontinuities. These patches may be manually selected and merged to shape the different faults within the survey. Distributions of the fault patches are generated in the form of histograms which serves to filter them by surface area, dip azimuth, dip magnitude and height, among others.

A general workflow for the automatic fault extraction is displayed on Figure 20. First, from an amplitude volume, I compute coherence or other edge enhancement attribute. Then, through the use of the directional Laplacian of a Gaussian, I enhance vertical and suppress horizontal features, which will be skeletonized in a subsequent step with an ant-tracking algorithm. The resulting fault patches are sorted by surface area, dip azimuth and dip magnitude. For this example I focused on surface area as the decisive parameter to filter patches. If the patches are too small, they will be rejected. Otherwise, I will merge them to recreate the manually picked faults

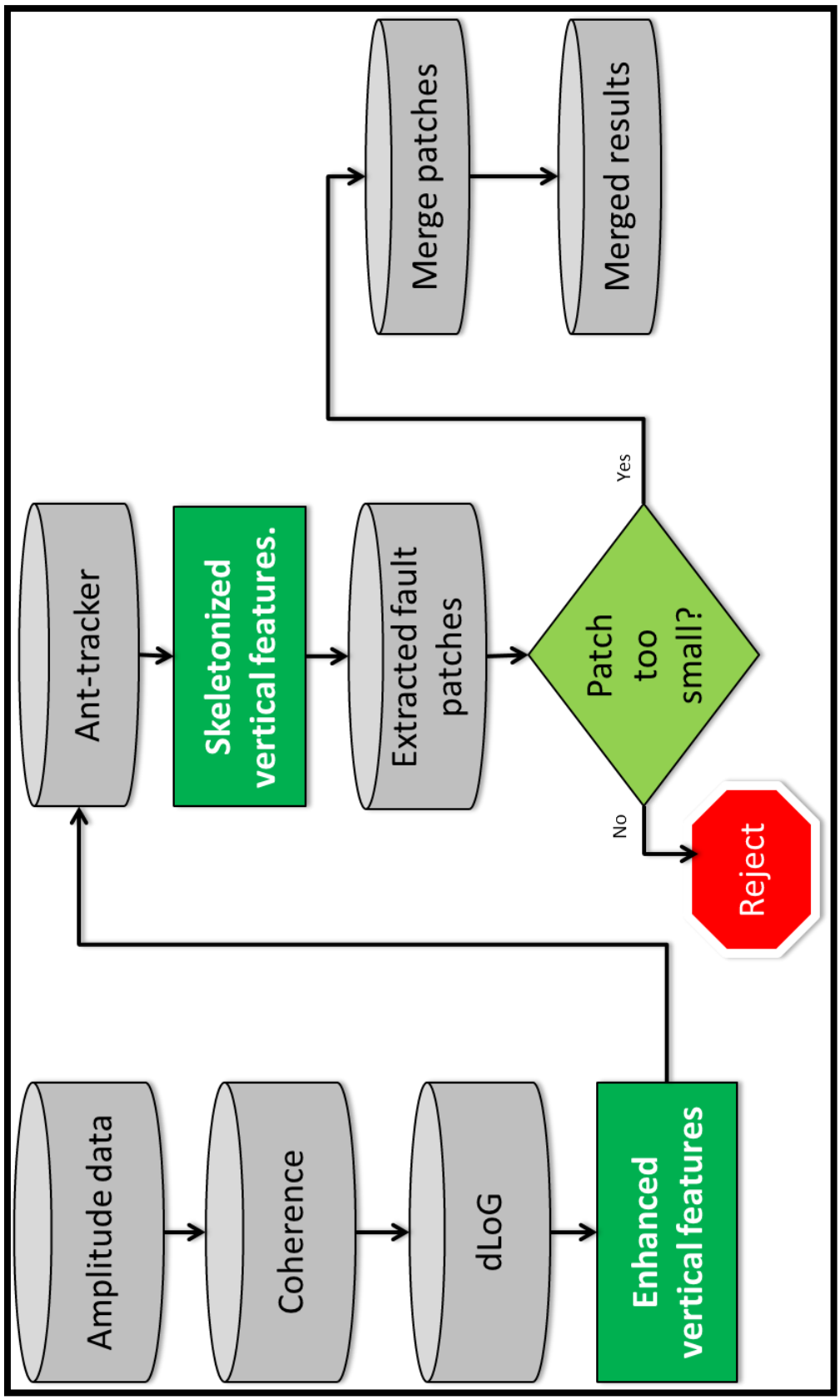

Figure 20. Workflow for automatic fault object extraction.

Using ant tracking for the attributes shown on Figures 16-19, fault patches were created and merged to recreate the faults that had already been manually picked. Figure 21 shows a visual and quantitative comparison of the fault patches generated. The histogram generated for each fault extraction process shows how the different algorithms affect its accuracy and effectiveness. The less the user needs to interact with the program, the more effective the workflow becomes in accelerating the fault definition process

Examining Figure 22a the dLoG input generates the least amount of patches. The dLoG patches are larger and more continuous, making the future merging process easier. In the case of variance, the image is fairly good, but gives rise to more small fault patches and lacks the continuity of dLoG, which results in a more difficult fault extraction. Finally, the energy ratio similarity is the attribute that yields the worst results, since its sensitivity to stratigraphic anomalies results in some horizontal artifacts, such that the manual merging step in the extraction process becomes much more difficult.

Analyzing the histograms on Figure 22 of the dLoG attribute note the percentage of small fault patches (<1000 m^2) is significantly smaller (about 30% of the patches) than for the energy ratio similarity. Likewise, the percentage of big fault patches (>5000 m^2) is significantly higher for the dLoG computation.

In a bid to quantify the effectiveness and advantages of each attribute for the fault extraction process, I created a surface out of each fault: first the manually picked and then the automatically extracted. Afterward, I subtracted the surface generated for each attribute from the one generated from the manually picked faults. Assuming that

the manually picked faults are closer to reality, the closer the subtraction approaches zero, the more accurate the automatic extraction was, thereby quantifying the attribute computation. The difference between the automatic fault extraction and the manually picked one has a significantly higher percentage of zeroes than the computed using the variance attribute. I did not consider the energy ratio similarity attribute for this comparison since it did not allow for a proper patch merging process.

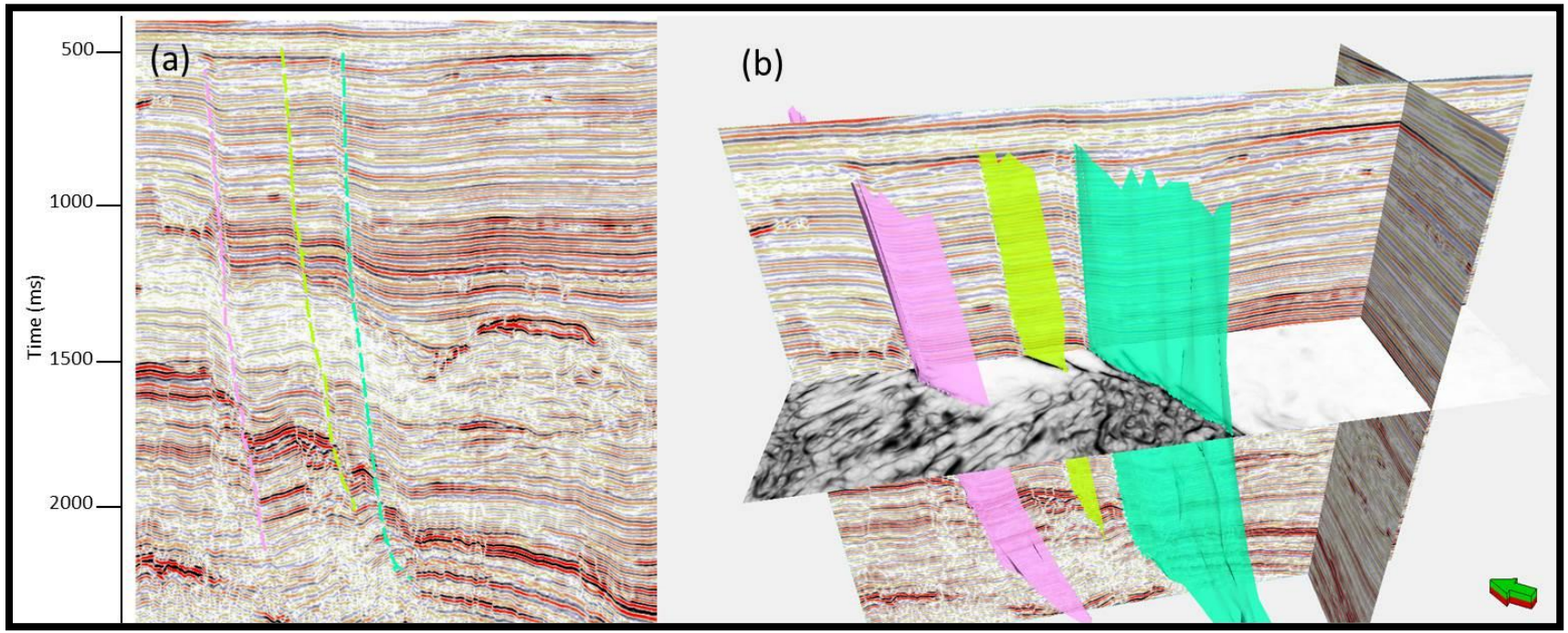

Figure 21 (a) Seismic cross-section showing three manually picked faults that are displayed (b) in 3D. Time slice is through the dLoG attribute fault probability.

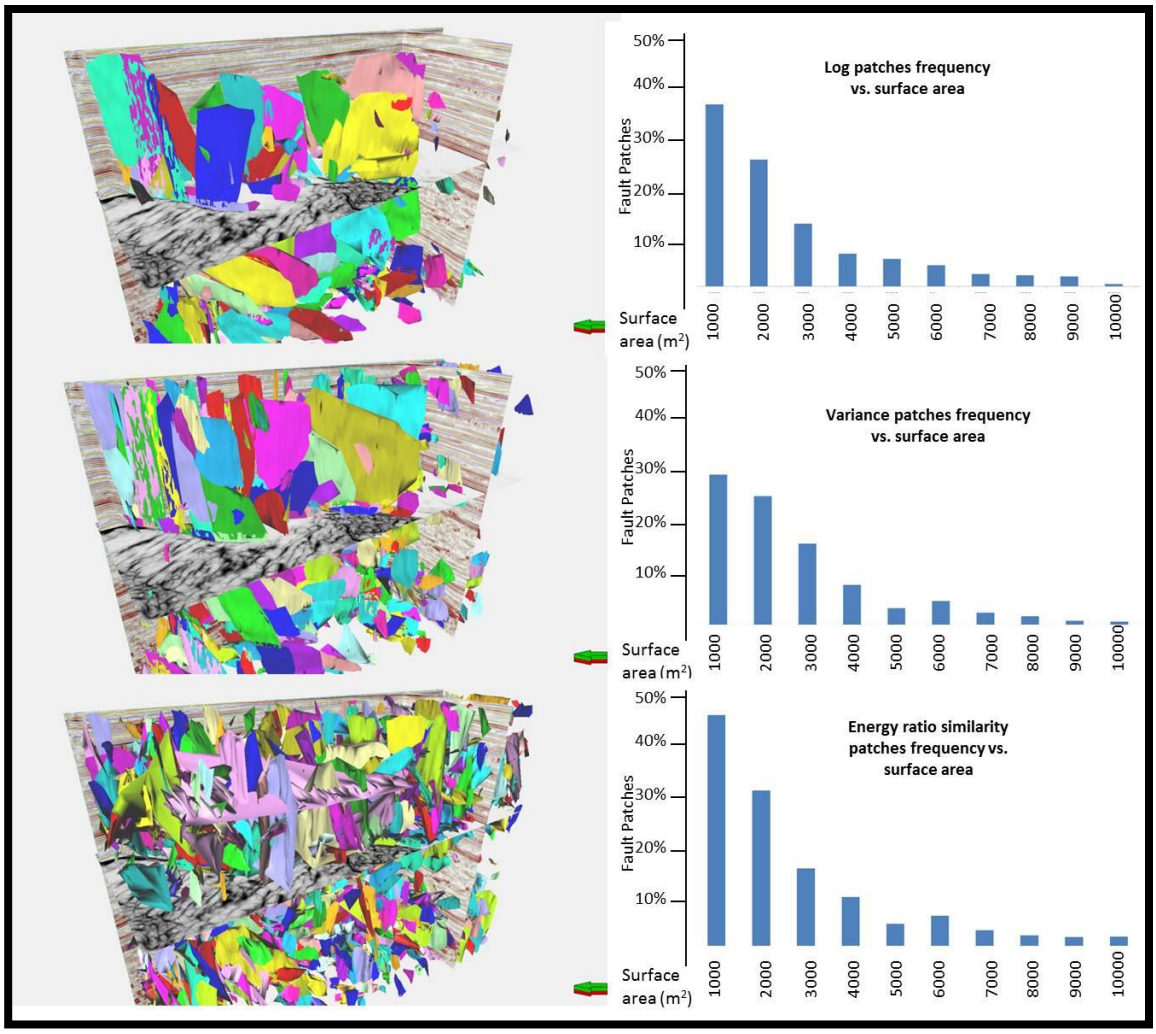

Figure 22. Fault extraction patches (left) for LoG, variance and energy ratio similarity. The histograms to the right represent the patches sorted by surface area.

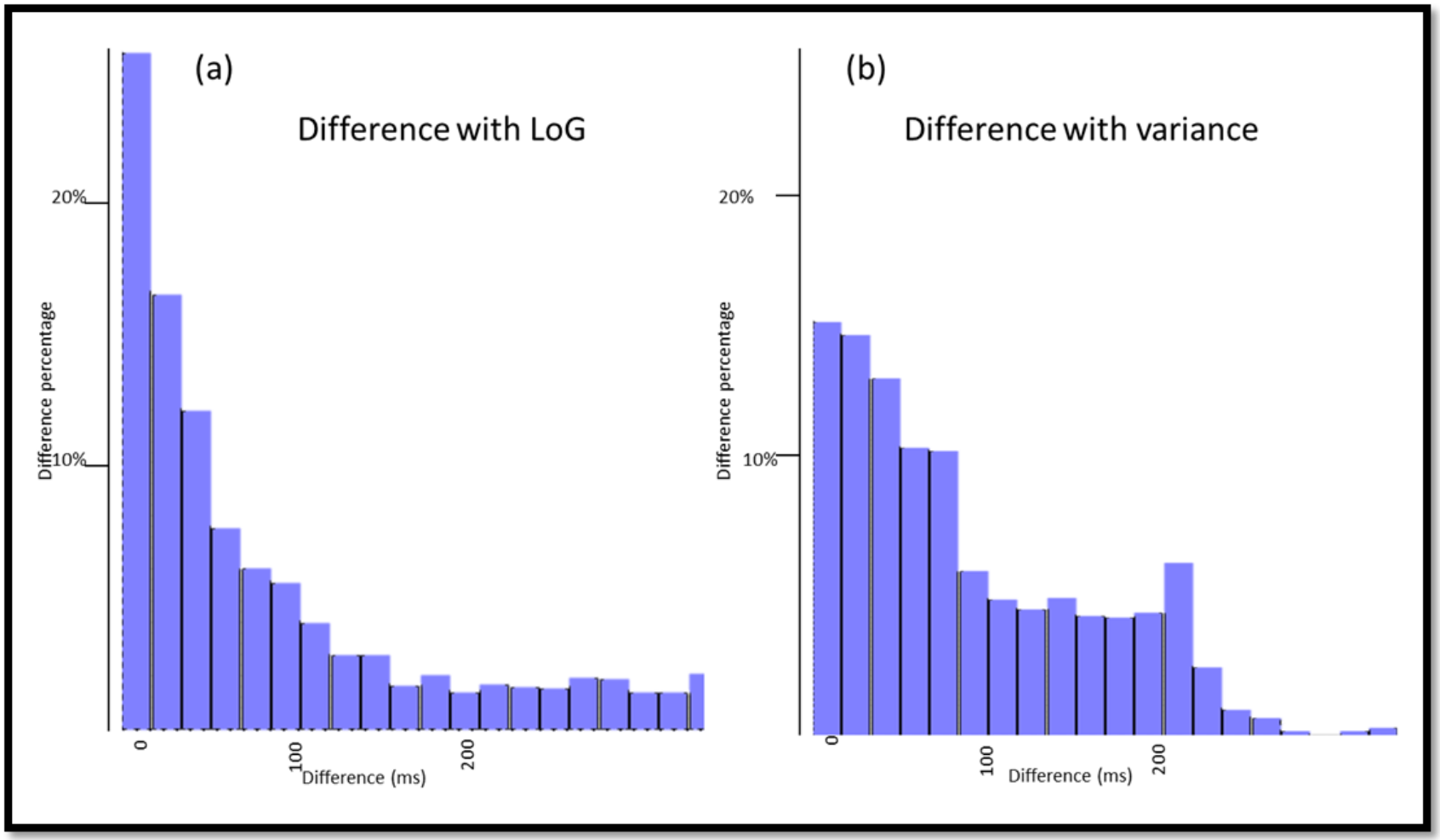

Figure 23. Histogram showing the similarity of computer-assisted fault extraction to manually extracted faults shown in Figure 21 for faults generated using (a) LoG and (b) variance.

Chapter 4: Conclusions

Fault image enhancement remains a pivotal objective in seismic data interpretation. Eigenvector analysis provides a means of volumetrically comparing the dip-magnitude and dip-azimuth of linear discontinuities. The directional Laplacian of a Gaussian sharpens fault images and improves fault continuity seen on the input coherence volume.

I thus have measures not only of strength of discontinuities but also of their orientation. Using such measures, I can reject or enhance geologic features and noise aligned with reflector dip, or generate image of faults that fall within an interpreter-defined azimuthal orientation. Such quantification of the orientation may facilitate statistical correlation of production to a given fault set or provide the anisotropic variogram used in geostatistical analysis of turbidite and fluvial deltaic deposits. Application of the same algorithm to curvature anomalies provides measures of dip and azimuth of axial planes.

Automatic fault extraction processes benefit from the application of this attribute enhancement. Not only do fault patches become more continuous and recognizable for merging and interpretation, noise removal improves the speed at which such computations may be performed. The accuracy of the process also becomes improved, as the automatically extracted faults closely resemble the reality represented by the manually picked faults.

References

Aare, V., and B. Wallet, 2011, A robust and compute-efficient variant of the Radon transform: GCSSEPM 31st Annual Bob. F. Perkins Research Conference on Seismic attributes – New views on seismic imaging: Their use in exploration and production, 550-586.

Barnes, A. E., 2006, A filter to improve seismic discontinuity data for fault interpretation: Geophysics, **71**, P1-P4.

Colorni, A., M. Dorigo, and V. Maniezzo, 1991, Distributed optimization by ant colonies: Proceedings of European Conference on Artificial Life, 134–142.

Dorigo, M., and L. M. Gambardella, 1997, Ant colony system: a cooperative learning approach to the traveling salesman problem: IEEE Transactions on Evolutionary Computation, 1, no. 1, 53– 66.

Great South-Canterbury Province. (2015, December 07). Retrieved May 07, 2016, from http://www.nzpam.govt.nz/cms/tools-and-servives/geoscience-exploration-data.

Iske, A., and Randen, T. (2005). Mathematical methods and modelling in hydrocarbon exploration and production. Berlin: Springer.

Machado, G., A. Abdulmohsen, B. Hutchinson, O. Oluwatobi, and K. Marfurt, 2016. Display and enhancement of volumetric fault images. Interpretation V 4, No. 1, pp, SB51- SB61

Marfurt. K, 2015, Techniques and best practices in multiattribute display: Interpretation, 1, B1-B23.

Marfurt, K. J., 2006: Robust estimates of reflector dip and azimuth: Geophysics, **71**, P29-P40.

Millán M. S., and E. Valencia, 2006, Color image sharpening inspired by human vision models: Applied Optics, 45, Issue 29, 7684-7697 doi.org/10.1364/AO.45.007684

Russell, B.H., 1989, Statics corrections – a tutorial: Canadian Geophysical Society, http://74.3.176.63/publications/recorder/1989/03mar/mar1989-statics-corrections.pdf., accessed 12 April, 2016.

Zhao, Y., Yue Y., Huang J., Yu Q., Liu Bingqing., and C. Liu 2015, Study and application of three parameters wavelet multi-scale ant tracking technology. SEG Technical Program Expanded Abstracts 2015: pp. 1866-1870.

Appendix: Geologic Background of the Great South Basin

The Great South Basin (GSB) is one of the largest basins of New Zealand, with a surface area of approximately 200000 km^2. The basin is a complex intracontinental of Cretaceous age failed rifts, evolving into subsiding basins during the Late Cretaceous and Paleocene. Figure A1 shows the areal extent of the Great South Basin, along with the Canterbury Basin to the north. The thickness approaches 6 km, which equals almost 20000 ft.

The basin has horst and grabens architecture, with plays that have been explored since the late 1960s including stratigraphic drape over basement highs, faulted anticlines, folds, turbidity channels, and basin floor fans, among others. Figure A2 shows a vertical cross section of the Great South Basin colored by the age of the sediments. All petroleum system elements are present in the basin (Figure A3).

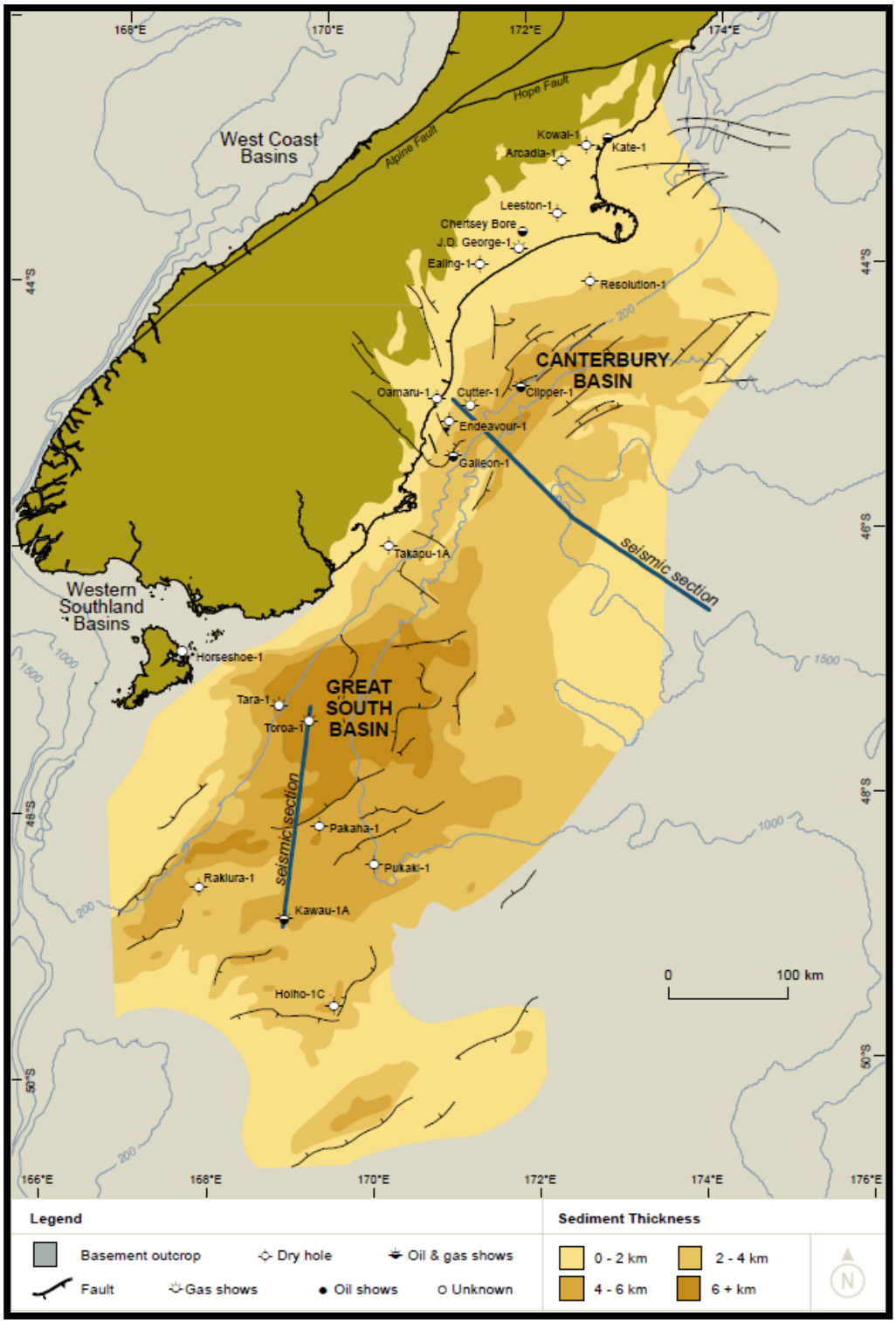

Figure A1 Location of Great South Basin. Thicknesses in the basin range from 0-6 km (from a New Zealand Petroleum and Mineral report, 2015).

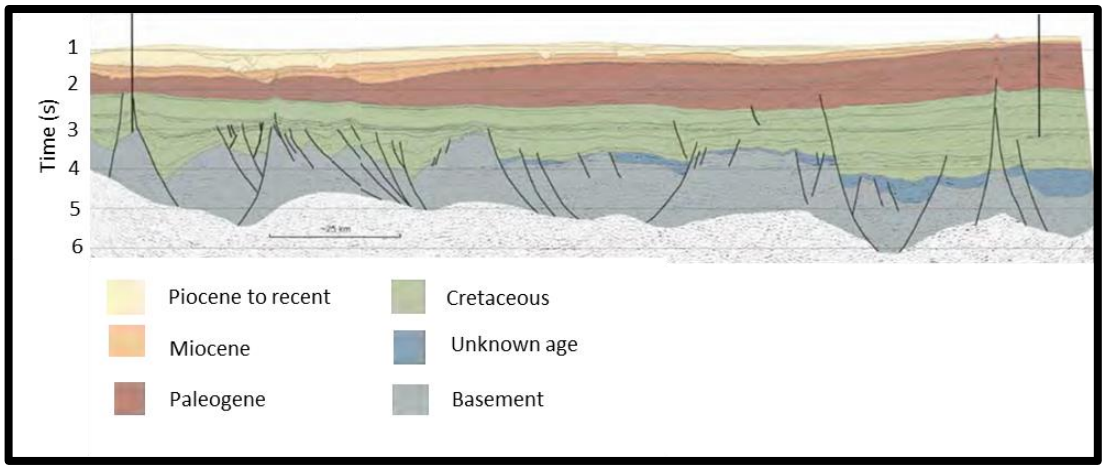

Figure A2. Vertical cross section of the Great South Basin with sediments colored by age of deposition (from a New Zealand Petroleum and Mineral report, 2015).

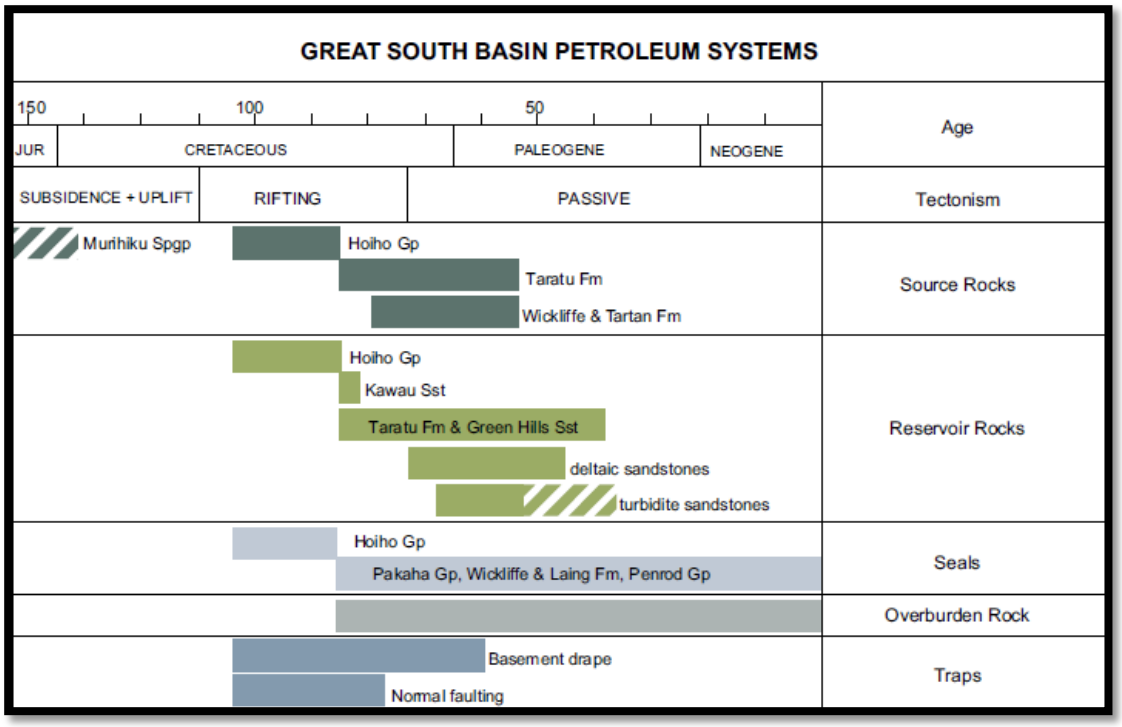

Figure A3. Petroleum system elements from the Great South Basin (from a New Zealand Petroleum and Mineral report, 2015).